DOKUZ EYLÜL UNIVERSITY
GRADUATE SCHOOL OF NATURAL AND APPLIED SCIENCE

INVESTIGATION OF COHERENT STRUCTURE OF TURBULENCE WITH WALL-NORMAL GRADIENTS OF THERMOPHYSICAL PROPERTIES

by
Çağrı Alim Seyit METİN

October, 2019
İZMİR

INVESTIGATION OF COHERENT STRUCTURE OF TURBULENCE WITH WALL-NORMAL GRADIENTS OF THERMOPHYSICAL PROPERTIES

A Thesis Submitted to the
Graduate School of Natural and Applied Sciences of Dokuz Eylül University
In Partial Fulfillment of the Requirements for the Degree of Master of Science
in Mechanical Engineering, Thermodynamics Program

by
Çağrı Alim Seyit METİN

October, 2019
İZMİR

M.Sc THESIS EXAMINATION RESULT FORM

We have read the thesis entitled **"INVESTIGATION OF COHERENT STRUCTURE OF TURBULENCE WITH WALL-NORMAL GRADIENTS OF THERMOPHYSICAL PROPERTIES"** completed by **ÇAĞRI ALİM SEYİT METİN** under supervision of **ASSOC. PROF. DR. MEHMET AKİF EZAN** and we certify that in our opinion it is fully adequate, in scope and in quality, as a thesis for the degree of Master of Science.

Assoc. Prof. Dr. Mehmet Akif EZAN

Supervisor

Asst. Prof. Dr. Sercan Acarer

(Jury Member)

Prof. Dr. Aytung EREK

(Jury Member)

Prof.Dr. Kadriye ERTEKİN

Director

Graduate School of Natural and Applied Sciences

ACKNOWLEDGEMENTS

I would like to thank my supervisor, Assoc. Prof. Dr. Mehmet Akif EZAN, for all his help, to conduct this research and his willing to teach which I always admire. This study would not have been possible without his valuable assistance. I also thank Prof. Dr. Stavros TAVOULARIS for his valuable contributions.

Foremost, I would like to thank my parents Alim and Gülsen METİN, and also my brother, Abdullah METİN,and additionally to my sisters, Sude and Naile METİN, for their endless support for my graduate study. I always feel privileged to have such a family that whenever I need help, they support me. I wish to express my gratitude to them because of their patience.

Finally, I would like to thank all my friends. I always feel their endless support. Especially, I would like to thank my friend Ayça ATAMTÜRK, because of her all helps and endless support from initial to end of the study.

Çağrı Alim Seyit METİN

INVESTIGATION OF COHERENT STRUCTURE OF TURBULENCE WITH WALL-NORMAL GRADIENTS OF THERMOPHYSICAL PROPERTIES

ABSTRACT

Coherent vortical structures have major responsibility for friction losses and heat transfer in wall-bounded turbulent flows, yet the hairpin vortex theory has been well-founded for boundary layer flows in recent decades. However, the modeling of buoyancy-driven turbulent flows has remained challenging, and existing models would poorly predict the effects of buoyancy. Here we show that the hairpin vortices in turbulent buoyancy-driven boundary layer consistently point the upstream direction of flow instead of downstream, and this characteristic is intrinsic vortex behavior for buoyancy-driven flow. We uncover that the coherent vortices straddle high-speed streak instead of low-speed streak; moreover, the quadrant of the tangential Reynolds shear stresses, one of the most important terms for the Reynolds-averaging models, dominates the first and third quadrant instead of the second and fourth one. These findings may help to improve our understanding of buoyancy-driven flow and buoyancy effects in turbulent models. The most important of all, the theory of anti-hairpin vortex is established through the present study.

Keywords: Anti-hairpin vortex, bouyancy-driven turbulent boundary layer, coherent vortical structures

TERMOFİZİKSEL GRADYENİNE SAHİP DUVARDA DÜZENLİ TÜRBÜLANS YAPILARININ İNCELENMESİ

ÖZ

Son yıllarda Reynolds ortalamalı Navier-Stokes (RANS) modelleri gelişmekte ve saç tokası girdap teorisi, düzenli girdap yapıların sürtünme kayıpları ve duvarla sınırlı türbülansta ısı transferi için büyük önem taşıdığı için sınır tabaka akışları için iyi bir alt yapı oluşturmaktadır. Bununla birlikte, doğal taşınımda türbülanslı akışların modellenmesi zorlayıcı olmaya devam etmektedir ve mevcut modeller doğal taşınım etkisinin öngörememektedir. Buçalışma kapsamında, türbülanslıdogal taşınım sınır tabakası akışındaki saç tokası girdaplarının sürekli olarak akış yönünde değil ters yönde yöneldiğini ve bu karakteristiğin dogal taşınımlı akış için özgün bir girdap davranışı olduğunu göstermektedir. Düzenli girdapları, düşük hızlı akışalanı yerine yüksek hızlı akış alanı üzerinde oturttuğu; dahası, RANS modeller için en önemli terim olan teğetsel Reynolds kayma gerilmesinin ikinci ve dördüncü terimi yerine birinci ve üçüncü teriminin hakim olduğu bulunmuştur. Bu bulgular, türbülans modellerinde doğal taşınım kaynaklı akış ve taşınım etkileri üzerinde bilgimizi geliştirmemize yardımcı olabilir. Hepsinden önemlisi, saç tokası girdap teorisinin eksik olan kısmı, ters saç tokası girdap teorisi, bu çalışma kapsamında belirlenmiştir.

Anahtar sözcükler: Ters saç tokası girdabı, doğal taşınımla türbülanslı sınır tabaka, düzenli girdap yapıları

CONTENTS

LIST OF FIGURES

LIST OF TABLES

CHAPTER ONE
BACKGROUND

1.1 Transition Boundary Layer

The pipe flow experiment by Osborne Reynolds in 1883 was observed on the visualization of a well-ordered flow along the pipe at small Reynolds number (1883). Further downstream of the pipe, the flow no longer prevents the ordered motion and becomes strongly mixing layers throughout the pipe. The critical Reynolds number, Re_{crit}, was introduced by Reynolds (1883) to distinguish these two regimes, which are called laminar and turbulent flow regimes. As the Reynolds number increases and becomes bigger than the critical Reynolds number, the characteristics of turbulent flow are identified with irregular and random motion, three-dimensionality, fluctuation, diffusive, and dissipative structures.

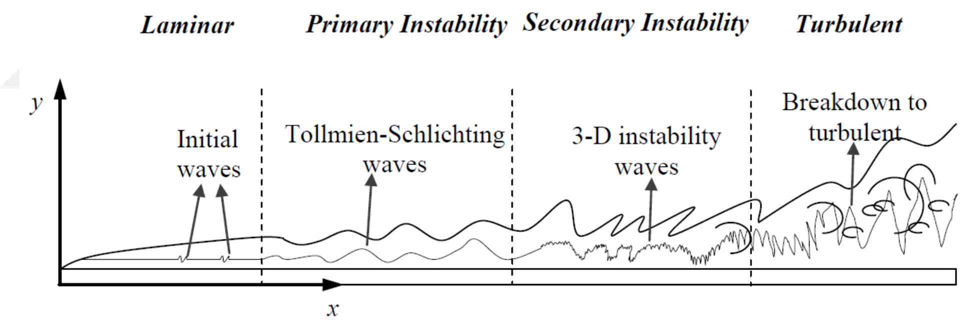

Figure 1.1 Sketch of zero-pressure-gradient laminar-transition-turbulent boundary layer flow on a flat plate

Transition, also called the onset of turbulence, occurs as the flow regime transforms from laminar flow to turbulent (Figure 1.1). The regime exists with a small disturbance at the Reynolds number above the critical Reynolds number. The transition regime is triggered with a small disturbance at the Reynolds number above the critical Reynolds number (Figure 1.1). Disturbance in the free stream, such as sound or vibration ribbon (Schubauer & Klebanoff, 1948) may enter the boundary layer as steady and/or unsteady fluctuations. This part of the process is called *Receptivity* (Morkovin, 1969). These disturbances may be produced by the pressure gradient of the outer flow, surface roughness, and level of turbulence intensity. Some mechanism of transition flow regime is still a mystery in literature (Wu, Adrian & Baltzer, 2015). Even though there are some disturbances within the flow, the flow can remain as laminar when the Reynolds number is less than the critical limit. That is, the transition boundary layer is not encountered in all types of disturbances since below a critical Reynolds number, the damping effect of the viscosity is high enough to prevent transient flow regime.

Two types of transient flows are known in literature; natural and bypass transitions. The natural transition is related to the boundary layer instability, amplification of the disturbances and the interaction of different stability modes (Kachanov, 1994). This instability mechanism is observed small and weak disturbances (Saric, Reed, & Kerschen, 2002). The bypass transition is related to nonlinear laminar flow breakdown under the influence of forced disturbance (Kachanov, 1994). It occurs when a strong disturbance which passes the growth of linear disturbance (Morkovin, 1969). The bypass transition mechanism observed in the case of roughness elements and/or high free-stream turbulence (Kachanov, 1994; Saric et al., 2002).

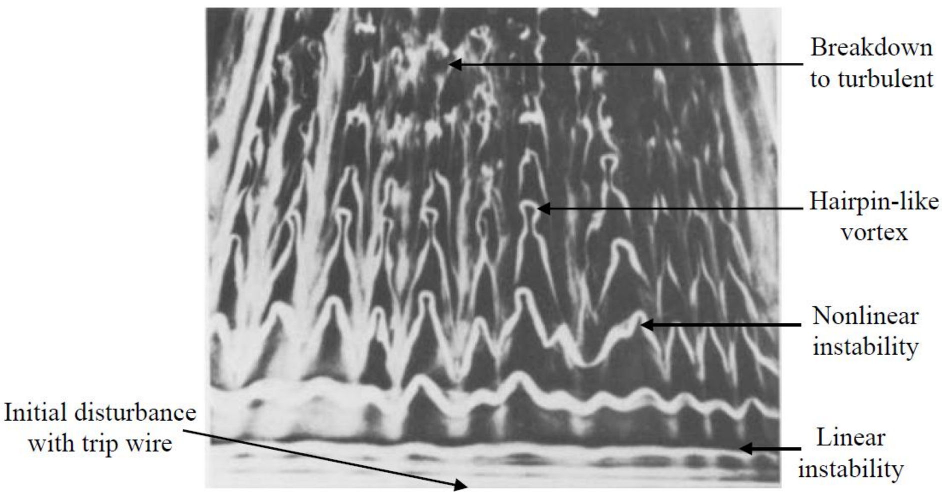

Figure 1.2 Smoke-wire visualization of the transition flow Perry et al. (1981)

The transition flow can be classified four main stages that are *receptivity*, *linear region*, *nonlinear region*, and *breakdown* (Figure 1.2). Receptivity is associated with the initial disturbance in the region of relatively smaller local Reynolds number, and it generates Tollmien–Schlichting waves. Receptivity phenomena can roughly be grouped into two categories. The first one is the disturbances that are initialized within the boundary layer. Secondly, the disturbances are produced away from the boundary layer, and they generate free-stream disturbances to affect the boundary layer instability waves (Goldstein & Lennart, 1989). In addition, receptivity also relates with a natural disturbance or an artificial forcing disturbance such as a wall-normal jet (Yaras, 2007), vibrating ribbon or localized suction/blowing modes (Saric et al., 2002). The initial growth of disturbance is described by linear stability theory of primary modes (Saric et al., 2002; Reed & Saric, 1989). The linear growth of the primary instability also called Tollmien–Schlichting waves continue in two-dimensional waves, which have small amplitude and the growth has weak propagation along the streamwise direction. The nonlinear growth instability mechanism occurs when the amplitude of disturbances reach sufficiently higher value. The flow is transformed into secondary instability which is more complicated involves three-dimensional effects. The nonlinear instabilities are observed when the amplitudes of instability waves reach values of order 1-2% of the free stream velocity (Kachanov, 1994). The growth of the secondary instability mechanism of the transient flow generates algebraic growth and then decays exponentially (Brinkerhoff & Yaras, 2015). The vortices on the streamwise and wall-normal direction become important (Saric, 2002). The three-dimensional secondary instability produces to lambda-shaped (Λ) vortices in the streamwise-spanwise plane. And then, the breakdown stage observes higher-order instabilities cause to turbulent flow. The Λ vortices are replaced by a hairpin-like vortex, which lifts the heads away from the wall. The hairpin-like vortex is noticed at the stage which promotes from the transition to turbulent boundary layer. The investigation and explanation of transition flow are associated with coherent turbulent structures in the boundary layer flow.

1.2 Coherent Turbulent Structures

The turbulent flow has chaotic, randomness in time and space, an irregular and wide range of time and length scale of mixing activities. However, it can possess a general characteristic for long enough time periods that the time-averaged statistics can be applied in the flow pattern. The identification of the coherent turbulent structure reveals the mechanism of the flow phenomena, explaining transition process in the laminar boundary layer flow, and achieves efficiently engineering products like reducing drag in a turbulent boundary flow, improving the noise reduction, increasing the aerodynamics performance and providing highly maneuverable flight.

The coherent turbulent structure was first discovered by Emmons (1951) with a tiny spot of turbulence appeared at some random position in the laminar boundary layer flow. The observation was also presented the turbulent spot, or turbulent source is a small and irregular shape and, growth straight angle to produce locally turbulent areas. The characteristic of the turbulent spot, which observes the velocity of the turbulent spot various from a value of $0.88U_\infty$ to U_∞ where U_∞ is the free stream velocity, appears suddenly and slowly move (Schubauer & Klebanoff, 1956). According to the experiments, the slower part of the turbulent spot augments to raise the leading edge of the turbulent spot. The shape of turbulent spot becomes staggered folds and conical shaped tails, accommodate in the hairpin-like shape of the turbulent spot which is initiated by Tollmien–Schlichting waves (Perry et al., 1981). Several configurations of the pattern have been identified the shape of the coherent turbulent structure such as Λ shaped or hairpin-like vortex.

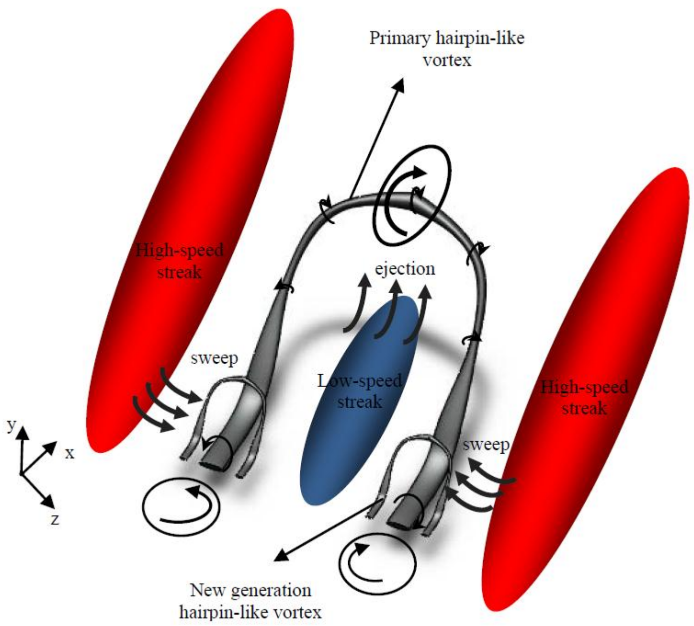

Figure 1.3 Schematic of a hairpin-like vortex

The hairpin-like vortices can be classified by various configurations such as symmetric, one-sided, or two-sided asymmetric vortices. The typical shape of hairpin-like vortex is leading edge of the spot lifts away from the wall, which overhangs a region in the laminar boundary layer (Schubauer & Klebanoff, 1956). This arrowhead-shaped edge pointed downstream (Singer & Joslin, 1994), while the arrowhead may point upstream in case of the dominant upper part of boundary layer disturbance (Yaras, 2007; Wu et al., 1999), which due to slow down in the leading part of the turbulent spot (Henningson et al., 1987). The primary hairpin-like vortices are formed by a low-speed streak. They sit above the higher-speed streak fluids, which induce a bump and elevates upward. The low-speed streak is associated with the stretched hairpin-like vortex with a strong vortices loop in the streamwise direction while the legs of the hairpin-like vortex exists a counter-rotating vortices pairs (Figure 1.3). The core vortex low-speed streak flow region between the legs of the hairpin-like vortex lifts away the head of the hairpin-like vortex from the wall, which is called *ejection* or *bursting*. The ejection of streak typically observed around y^+~10 (Pope, 2000). The low-speed streak from the ejection is fed by the high-speed streak region, is known as *sweep* (Corino & Brodkey, 1969). The head of the hairpin-like vortex elevates linearly from the wall, and low-speed streak flow region relates vortex loop in the region $5 < y^+ < 35$ (Smith & Metzler, 1983). The angle of the head of the hairpin-like vortices inclined at approximately less than 45^o from the wall. This phenomenon causes the convective velocity difference in the streamwise direction between the legs and head of the hairpin vortices. The velocity of the head of the hairpin-like vortices is typically $0.95U_\infty$ and for the legs of the hairpin-like vortices is about $0.5U_\infty$ (Brinkerhoff & Yaras; 2014). The angle of the inclined plane connecting to the heads of the hairpin-like vortices depends on the rate of the growth in wall-normal and spanwise directions, the convective speed of the hairpin-like vortices are in the streamwise direction, and to relate of the new generated hairpin-like vortices (Adrian et al., 2000). The shape of the hairpin-like vortices grows and stretches in time, generates the new hairpin-like vortices born close to the legs of the primary hairpin-like vortex when the hairpin-like is stretched sufficiently (Singer, 1996). In addition, the signature of the hairpin-like vortices may found in the outer layer of turbulent boundary and further distance above the boundary layer (Azih et al., 2012; Adrian et al., 2000; Perry & Chong, 1982). The length of the hairpin-like vortices can be extending over length of 2δ with a region of upward, which has large vortex cores (Ganapathisubramani et al., 2003).

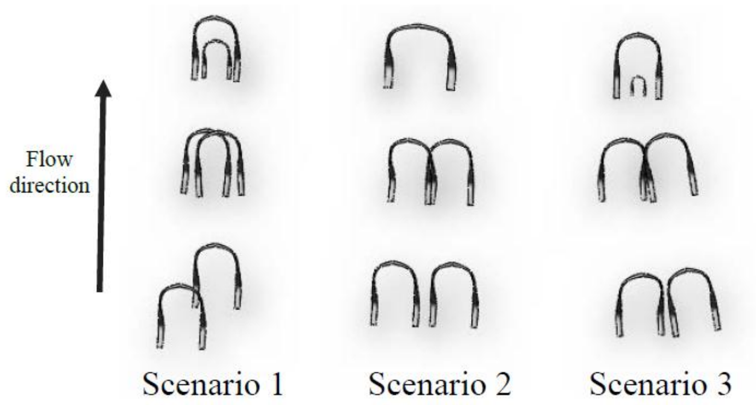

Figure 1.4 Idealized schematic of hairpin-like vortex merging scenarios

The various possibilities of the merging mechanism of the hairpin-like vortices may be configured (Figure 1.4). One of the idealized scenarios is that overlapped each other laterally with different convective speeds (Scenario 1). The result is that two hairpin-like vortices generated with larger and smaller ones (Tomkins & Adrian, 2003). Another merging mechanism is that the adjacent leg of the hairpin vortices merging only one vortex (Scenario 2) and, growing and stronger the hairpin-like vortex with convecting speed (Wark & Nagib, 1991). The shape of the hairpin-like vortex increases in the spanwise direction. Instead of the merging inner legs of the hairpin-like vortices, merging with the upper structure of hairpin-like vortices similar to the first merging mechanism but at this time (Scenario 3), the residual hairpin-like vortex rotates opposite of the mean shear (Tomkins & Adrian, 2003). The lateral growth mechanism of the hairpin-like vortex is also explained with merging of the hairpin-like vortices, which is associated low-speed streak flow region (Tomkins & Adrian, 2003). Otherwise, they may rapidly grow and break down to generation of new hairpin-like vortex without contact with the primary hairpin-like vortex (Gad-El-Hak et al., 1981).

The group of the hairpin-like vortices aligns the line of low-speed streak that is the locally distorted region grows within the laminar shear layer, which is progressed to the dominated the hairpin-like vortex. The hairpin-like vortices in the low-speed streak can be classified K-type and H-type hairpin-like vortices in the transition process. K-type transition is observed ordered formation each line of the hairpin-like vortices (Klebanoff et al., 1962). On the other hand, H-type transition is recognized asa staggered formation of the hairpin-like vortices (Herbert, 1983). These groups of the hairpin-like vortices organized into streamwise direction are also called wave packets. The turbulent wave packets expand exponentially to downstream and laterally at the same time (Asai &Nishioka, 1989). The number of hairpin-like vortices in the turbulent wave packets can be a various number with depends on the displacement-based Reynolds number. Two or three hairpin-like vortices accommodates within the wave packets at $Re_\delta \sim O(10^2)$ and four or five hairpin-like vortices at $Re_\delta \sim O(10^3)$ (Reinink & Yaras, 2015; Adrian et al., 2000).

CHAPTER TWO
INTRODUCTION

Buoyancy-driven flows are ubiquitous in nature and many engineering applications such as nuclear reactors (Chung et al., 2004) as well as nuclear safety during serious damage (Lee, Lee & Suh, 2007). or, electronic industry (Incropera, 1988). Moreover, many species in nature use updraughts to sustained static soaring for energy-efficient flight and choosing a particular flight path during seasonal migration (Shepard, Ross & Portugal, 2016). The investigation of flight dynamics and interaction with updraughts of those species may lead novel bio-inspired aircraft design that is highly maneuvrable and more efficient. From this perspective, this study focuses on vortex dynamics to shed light on the mechanism of turbulent natural convection that may help to improve the efficiency of those devices and increase our knowledge of nature.

Strong turbulent natural convection in an enclosed cavity has been receiving increasing attention over the last decades (Miroshnichenko & Sheremet, 2018); historically, the natural convection of the cavity has been studying for decades to now. Most of the former studies performed in the laminar regime (Markatos & Pericleous, 1984; de Vahl Davis, 1983; Inaba & Fukuda, 1984) or weakly turbulent (Brag a& Viskanta, 1992; Tian, & Karayiannis, 2000a; Tian & Karayiannis, 2000b; Chenoweth & Paolucci, 1986; Zhang et al., 2014) due to limited computational resources; conversely, the turbulent natural convection in the cavity had relied on experimental studies (Inaba & Fukuda, 1984; Lankford& Bejan, 1986; Braga& Viskanta, 1992; Schöpf & Patterson, 1995; Ivey, 1984). With increasing computational resources, researchers have been started to pay attention to strong turbulent flow at high Rayleigh numbers (Sebilleau et al., 2018; Ng et al., 2017; Kogawa et al., 2016). In those studies, turbulent natural convection in the cavity has been investigated in many different aspects. The budget of the Reynolds stresses and turbulent heat fluxes (Sebilleau et al., 2018; Barhaghi & Davidson, 2007; Versteegh & Nieuwstadt, 1998; Kizildag et al., 2014; Fedorovich & Shapiro, 2009), the budget of turbulent kinetic energy (Sebilleau et al., 2018; Barhaghi & Davidson, 2007), the budget of turbulent heat fluxes (Sebilleau et al., 2018; Barhaghi & Davidson, 2007), and the budget of temperature variances (Sebilleau et al., 2018) for the turbulent natural convection in the cavity are examined to assist the modelling of buoyancy effect, and statistical data for transition and turbulent boundary layer flows. Performance of the several subgrid-scale models also investigated during the transition and turbulent regimes (Lau et al., 2013). The Smagorinsky subgrid-scale model found dissipative to capture the transition region even for high resolution of grid (Barhaghi & Davidson, 2007). However, the wall adapting local-eddy viscosity and dynamic Smagorinsky models performed better prediction to capture the turbulent statistics and mean flow parameters (Kizildag et al., 2014; Barhaghi & Davidson, 2007). In case of a high Rayleigh number for a differentially heated cavity, overall, thin vertical boundary layer emerges near the walls, and a large stratified core area exists in the cavity center (Trias et al., 2007; Trias et al., 2010a). The steady motion of the vertical boundary layer on the upstream is triggered by Tollmien-Schlichting waves and produced violent ejection into the cavity core (Trias et al., 2010a; Xin & Le Quéré, 1995). Hook-like structures in the boundary layer emerge during the violent ejection that oscillates the internal waves in the core of the cavity (Xin & Le Quéré, 1995; Elder, 1965). Eventually, for high Rayleigh number, these transitional structures breakdown to turbulent in a significantly thickening the boundary layer (Trias et al., 2007; Trias et al., 2010b).

Coherent turbulent structures of the natural convection boundary layer have been investigated in a limited number of studies and need to be further research. More specifically, is the theory of the hairpin vortices in the canonical turbulent boundary layer is valid for the buoyancy-driven turbulent boundary layer? For Rayleigh number around 10^{11}, unstable spanwise vortices are observed in the upper part of the cavity; however, these vortices do not extend streamwise and wall-normal direction, therefore the hairpin-like vortices are not observed (Kogawa et al., 2016). For comparison, the streaky flow was observed in the buoyancy-driven boundary layer; further, the streaks become finer as Rayleigh number increases (Ng et al., 2017). The spanwise spacing of streaks was found 100-200 viscous wall units which are similar to the canonical turbulent boundary layer (Ng et al., 2017). We should remind that typical spanwise spacing of hairpin vortex is about 100 viscous wall unit and rides on the low-speed streaks (Adrian, 2007). However, the existence of streaks is not mean the existence of hairpin vortices (Lozano-Durán & Jiménez, 2014; Hack & Moin, 2018). On the other hand, transitional spanwise vortices in buoyancy-driven boundary layer eventually stretched out and generated the hairpin vortices (Barhaghi & Davidson, 2007). These coherent structures were also associated with the hot thermal plume from the hot wall (Sebilleau et al., 2018); moreover, conditional averaged structures were related with large temperature gradient fluctuation (Pallares et al., 2010). The inclined angle of these vortices was about 30º (Pallares et al., 2010) which is similar to the hairpin-like vortices in the canonical turbulent boundary layer. However, there are some open questions still exists, more abstract, can we observe the same mechanism: generation, growth, and interaction of structures that proposed in the hairpin-like vortex theory, or does the turbulent natural convection have intrinsic mechanism?

The purpose of this study is to examine the coherent turbulent structures in the buoyancy-driven turbulent boundary layer in a differentially heated cavity. In this approach, we conducted a Direct Numerical Simulation at Rayleigh number 1.58×10^9 for air. In particular, the emphasis is placed on the examination of the origin and interaction of the hairpin-like vortices in the buoyancy-driven turbulent boundary layer in quasi-deterministic point of view (Robinson, 1991). In this approach, we focuses on kinematic description of vortical structures as well as the elucidation of how they related to heat transfer and skin friction stress on the bouyancy-driven turbulent flow (Lozano-Durán, Flores & Jiménez, 2012).

CHAPTER THREE
COMPUTATIONAL METHOD

In the present study, a direct numerical simulation was performed on turbulent natural convection in a differentially heated cavity. The working fluid is air, modeled as subsonic compressible flow and natural convection is represented by density variation with temperature. The sides wall of the square cavity is maintained isothermally at a constant temperature while the front and back faces are set to periodicity. Initially, the computational domain is stationary and motion of fluid introduced by buoyancy. The computational domain has sufficient refined to Kolmogorov scales by finite volume structured grids to capture spatial and temporal turbulent structure within the boundary layer. The non-dissipative second-order centered difference scheme is applied to advection and diffusion terms on the governing equations while the second-order backward difference scheme is used for time marching. The discretized governing equations are solved implicitly with the Pressure Implicit with Splitting of Operator (PISO) algorithm. Subsequent sections are elaborately discussed the computational strategy.

3.1 Computational Domain

Three-dimensional turbulent natural convection is investigated with the direct numerical simulation in a differentially heated cavity which is same as experiment by Ampofo & Karayiannis (2003), which is reproduced in this study. The aspect ratio, height/width, of the cavity is 1. The uniform constant temperature is applied to the sides wall of the cavity to simulate the heating and cooling effect. The left vertical wall of the cavity (y/H=0) is exposed to hot temperature (T_H = 50 ^{o}C); meanwhile, the right vertical wall (y/H=0.2) is subjected to cold temperature (T_C = 10 ^{o}C). The dimensions of cavity are $L_x = L_y = H$ and $L_z = 0.2H$ in the streamwise (x-), wall-normal (y-) and spanwise (z-) direction, respectively (Figure 3.1). The periodic spanwise dimension of the cavity is adjusted minimum dimension that able to capture turbulent structures in the side walls boundary layer to reduce the computational cost (Barhaghi & Davidson, 2007; Kizildag et al., 2014). The

Rayleigh numbers based on height and width of the cavity are $Ra_x = g\beta(T_H - T_C)L_x^3Pr/\nu^2 = 1.58 \times 10^9$, where g is the standard acceleration due to gravity, β is the thermal expansion coefficient, and ν is the kinematic viscosity, and Pr is the Prandtl number to air. The differentially heated cavity is filled with air which is assumed compressible Newtonian fluid. The summary of the material properties of the working fluid and the standard gravity are provided in Table 3.1.

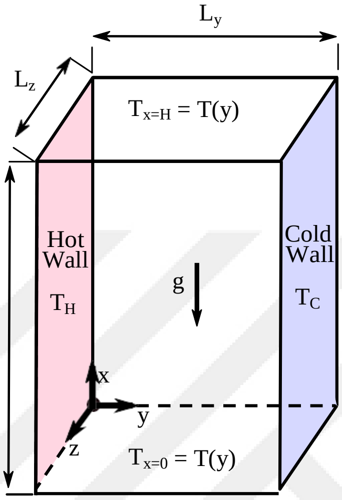

Figure 3.1 Schematic representation of the computational domain

Table 3.1 Standard gravity and thermophysical properties of air at 30°C

Material	Standart gravity **g** (m/s^2)	Dynamic viscosity μ (kg/m.s)	Prandtl number Pr (-)
Air	-9.81**i**+0**j**+0**k**	1.87×10^{-5}	0.71

3.2 Boundary and Initial Conditions

The top, bottom, and side walls of the cavity are applied no-slip boundary condition for momentum equation while periodic boundary condition is imposed on the spanwise direction for all governing equations. The periodic boundary conditions can be employed under consideration of the infinite depth of the cavity in the spanwise direction. This assumption is only valid as long as the largest coherent turbulent structures can be accommodated in the computational domain. Kizildag et al. (2014), and Barhaghi & Davidson (2007) showed that 0.1H and 0.2H spanwise length of the cavity to be sufficient for the natural convection turbulent boundary layer. The hot and cold wall of the cavity are kept uniform at constant temperatures such that $T_H = T_{init} + 0.5\Delta T$ and $T_C = T_{init} - 0.5\Delta T$, respectively, where $T_{init} = (T_H + T_C)/2$ is the initial temperature in the cavity, and $\Delta T = T_H - T_C$ is the temperature difference between the hot and cold walls. The linear temperature profile is imposed for the top and bottom walls of the cavity for the energy equation. This boundary condition is a more realistic representation of the experimental study than the adiabatic boundary condition (Sebilleau et al., 2018). Both boundary conditions were applied in the preliminary study, and turbulent statistics showed that the linear temperature boundary condition leads to more close results to the experiments. Also, the turbulence level with the linear temperature variation has kept higher whereas the adiabatic boundary condition damped the turbulence (Sebilleau et al., 2018).

Initially, the working fluid is stationary in the cavity, and the initial temperature is set to the average temperature of the hot and cold walls with a spatially uniform. The initial vortical structures and the transitional period from the initial condition to the turbulent equilibrium state are not subject to this study; therefore, statistical data of turbulent flow is collected after reaching stationary turbulent flow. The statistics of turbulent flow are accumulated 10 Flow Through Time (*FTT*) (Komen et al., 2017), which is defined as,

$$FTT = \frac{L_x}{u_{max}} \tag{3.1}$$

where u_{max} is the maximum velocity in the natural convection boundary layer on the side walls. The statistical data are also confirmed with checking the variation of data at every 10 *FTT*s that it is confirmed the turbulent flow reached statistical equilibrium.

3.3 Spatial and Temporal Resolution

Structured hexahedral finite-volume grids are generated over the computational domain. The spatial and temporal cells are adequately small enough to capture desired eddies which scale on Kolmogorov micro length, η, for the direct numerical simulation. The viscous length scale, δ_v, is employed to normalize the spatial dimensions,

$$\delta_\upsilon = \frac{\upsilon}{u_\tau} \tag{3.2}$$

and

$$u_\tau = \left(\frac{\tau_w}{\rho}\right)^{0.5} \tag{3.3}$$

where υ and ρ are the kinematic viscosity and density of working fluid, τ_w is the wall shear stress and u_τ is the friction velocity at the wall. The "+" superscript is used to represent the normalization by the viscous length scale for the spatial and temporal dimensions. And, the temporal resolution normalised by u_τ and υ as described below,

$$\Delta t^+ = \Delta t \frac{{u_\tau}^2}{\upsilon} \tag{3.4}$$

The smallest scale turbulent structure is generally the order of $\eta^+ \approx 2$ for a wall-bounded turbulent shear layer. In the experimental study by Ampofo & Karayiannis (2003), the corresponding Kolmogorov length scale was found 0.4 mm at about mid-height of the cavity. Similarly in the experiments, the viscous length scale and the friction velocity at the mid-height of the cavity are chosen a reference scale, and the properties in Table 3.2 normalized that values. Table 3.2 provides a summary of the spatial and temporal resolutions. The spatial resolution in the periodic spanwise direction is distributed uniformly $\Delta z^+ = 10$. In the streamwise direction, maximum spatial resolution is set to $\Delta x^+ < 8$ in the vicinity of the middle of the cavity. The streamwise spatial resolution is refined near the top and bottom wall, $\Delta x^+ < 1$, to resolve the boundary layer at these walls. The finite volume grids are increasing 1.024 cell-to-cell expansion at a constant rate from the wall to the middle of the cavity. A similar approach is applied to the bottom wall. The first cell height from the side walls is placed at $y^+ < 1$ and the finite volume cells are stretched 1.009 cell-to-cell increments at a constant rate until the mid-plane of the cavity.

Table 3.2 The spatial and temporal resolution

$N_x \times N_y \times N_z$	Δx^+	Δz^+	y^+	Δt^+
366 × 186 × 72	< 8	10	< 1	0.4

The accuracy of temporal resolution is also important to capture the coherent structures as well as spatial resolution (Georgiadis, Rizzetta & Fureby, 2010). The larger time step may cause unphysical effects such as producing numerical dissipation errors and decay turbulent vortical structures. It is suggested that the time step in wall units should be smaller than unity, $\Delta t^+ < 1$, for canonical turbulent flows, which denotes to the viscous time scale in the sublayer (Georgiadis, Rizzetta & Fureby, 2010). The accuracy of different time scale was also performed in terms of the velocity and vorticity fluctuation, and Reynolds stresses profile by Choi and Moin (1994). It is suggested that the time step in wall units $\Delta t^+=0.4$ is sufficiently enough to resolve turbulent statistics. In addition to the physical restriction for the time step, numerical stability also plays an important role in the accuracy of results; so that reason, it could be argued that the Courant Friedrichs Lewy (CFL) number should be kept below 0.5. Thus, consideration of physical and numerical constrained, the time step size is set to $\Delta t^+ = 0.4$ with a constant interval which corresponds to the maximum CFL = 0.2 during the simulation.

3.4 Governing Equations and Solution Methods

The open-source finite volume software, OpenFOAM 5.x, is used to solve the time-dependent, compressible, strong-conservative form of mass, momentum and energy equations (Patankar, 1980). The Newtonian viscous flow is assuming by neglecting thermal radiation. The governing equations read for,

Conservation of Mass:

$$\frac{\partial \rho}{\partial t} + \frac{\partial(\rho u_j)}{\partial x_j} = 0 \tag{3.5}$$

Conservation of Momentum:

$$\frac{\partial(\rho u_i)}{\partial t} + \frac{\partial(\rho u_j u_i)}{\partial x_j} = -\frac{\partial p}{\partial x_i} + \frac{\partial \tau_{ij}}{\partial x_j} + \rho g_i \tag{3.6}$$

Conservation of Energy:

$$\frac{\partial(\rho h_0)}{\partial t} + \frac{\partial(\rho u_j h_0)}{\partial x_j} = \frac{\partial p}{\partial t} + \frac{\partial}{\partial x_j}\left(k \frac{\partial T}{\partial x_j}\right) + \frac{\partial(u_i \tau_{ij})}{\partial x_j} + \rho g_i u_i \tag{3.7}$$

where τ_{ij},

$$\tau_{ij} = \left(\mu\left(\frac{\partial u_i}{\partial x_j} + \frac{\partial u_j}{\partial x_i} - \frac{2}{3}\frac{\partial u_k}{\partial x_j}\delta_{ij}\right)\right) \tag{3.8}$$

and, Einstein summation is used for the index notation i, j, k = 1, 2, 3 that represents streamwise, wall-normal and spanwise directions, respectively. δ_{ij} is the Kronecker delta, and the bulk viscosity coefficients omitted (Stokes' hypothesis).

The governing equations are discretized with second-order centered differencing of the spatial derivatives and second-order backward differencing of the temporal derivatives. The reason for using the centered differencing scheme for the spatial derivatives is to eliminate the numerical dissipation errors. However, it may cause dispersion error and oscillation of the variables for high Peclect numbers. In the case of the direct numerical simulation, the finer spatial resolution reduces Peclect number small enough that produces negligible dispersion errors (Barhaghi & Davidson, 2007). The Pressure Implicit with Splitting of Operator (PISO) algorithm is applied for the pressure-velocity treatment of the time-dependent flow. For the solution of the linear set of algebraic equations, a Preconditioned Conjugate Gradient (PCG) solver is applied to the pressure equation together with Geometric-Algebraic Multi-Grid (GAMG) solver for pre-conditioning (Jasak, Jemcov & Tukovic, 2007a; Jasak, Jemcov & Tukovic, 2007b; Jemcov, Maruszewski & Jasak, 2007). A Preconditioned Bi-Conjugate Gradient (PBiCG) solver is also used for the momentum equations with Diagonal-based Incomplete LU (DILU) for preconditioning. The root-mean-square of the normalized tolerance for the solution of pressure and momentum equations are reduced to 10^{-9} for momentum and pressure equations. The numerical study is performed in Intel Xeon Scalable 6148 processors at TUBITAK ULAKBIM, High Performance, and Grid Computing Center.

3.5 Validation of the Numerical Study

The experimental study by Ampofo and Karayiannis (2006) was reproduced to validate first- and second-order statistics of the turbulent natural convection, which is the same case in this study which examined in the anti-hairpin vortices. In Figure 3.2, the first-order statistics (mean temperature, and mean streamwise and wall-normal velocity) compared to the experimental data at the mid-height of the cavity. The mean temperature and streamwise velocity component present excellent agreement against the experimental results. The mean wall-normal velocity can capture favorably to the general behavior of the profile. However, the mean wall-normal velocity component undershot the experimental data in the inner layer while it overshot the experimental data in the outer layer. This may be related to the top and bottom temperature boundary conditions. In the experimental study, the side wall temperature maintained by pumping hot and cold water flow to chambers that attached to the side walls (Ampofo & Karayiannis, 2006). Meanwhile, the top and bottom walls of the cavity made of high conducting mild sheet steel that produces a non-linear temperature profile between the side walls. The temperature variation in the cavity surfaces may lead to over- or undershoot the profile that shown more prominent in the wall-normal component of the first-order (Figure 3.2c) and second-order statistics (Figure 3.3c).

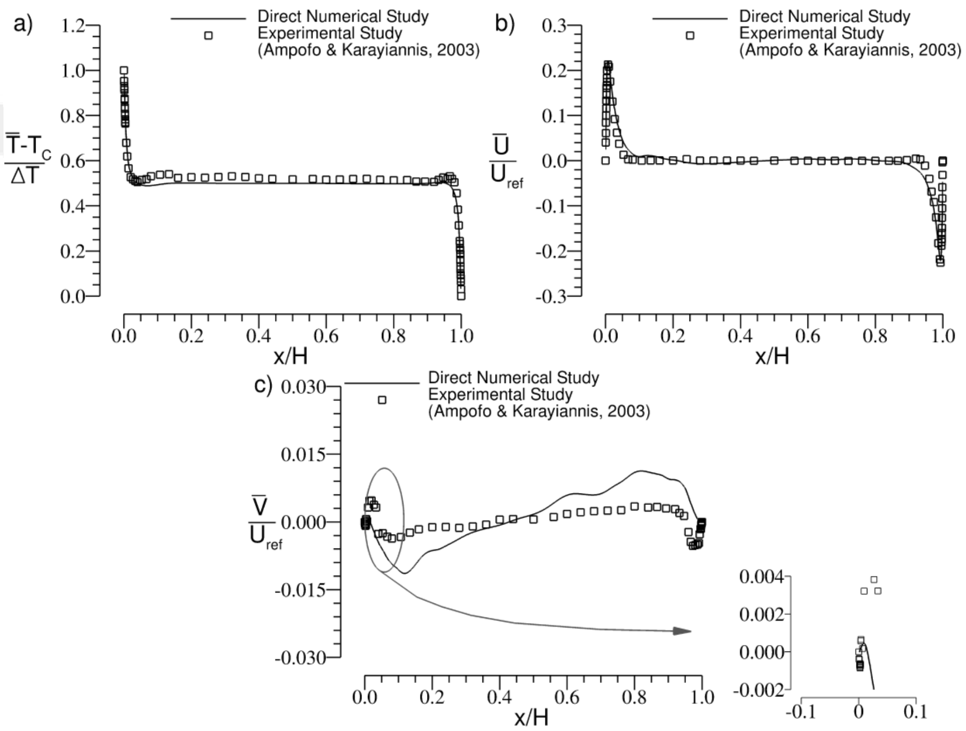

Figure 3.2 First order statistics validation of the numerical study

Likewise, the second-order statistics of flow data compared to the experimen- tal results. The root-mean-squared of the temperature fluctuation, t_{rms}, in the boundary layer satisfactory agreement with the experimental profile yet the peak value of the temperature fluctuation is underestimated (Figure 3.3a). On the other hand, the temperature fluctuation in the center of the cavity is favorably agreed to the experiment. The root-mean-squared streamwise velocity fluctuation, u_{rms}, (Figure 3.3b), the root-mean-squared wall-normal velocity fluctuation, v_{rms}, (Figure 3.3c) and the mean cross-correlated streamwise and wall-normal velocity fluctuations, uv,

(Figure 3.3d) show excellent agreement to the experiment in the boundary layer. However, the deviation on the root-mean-squared fluctuation profiles except the temperature becomes fairly agreed to the experiment in the center of the cavity, and the difference becomes more prominent for the root-mean-squared wall-normal velocity fluctuation (Figure 3.3c). Overall, the second-order statistics are captured very well in the boundary layer; meanwhile, some deviation occurs in the middle of the cavity. As a result, the difference between the numerical and experimental study is quite small in the boundary layer and this could not change the vortex dynamics or behavior of the anti- hairpins proposed as the main outcome of this study, but this may affect of the vortices.

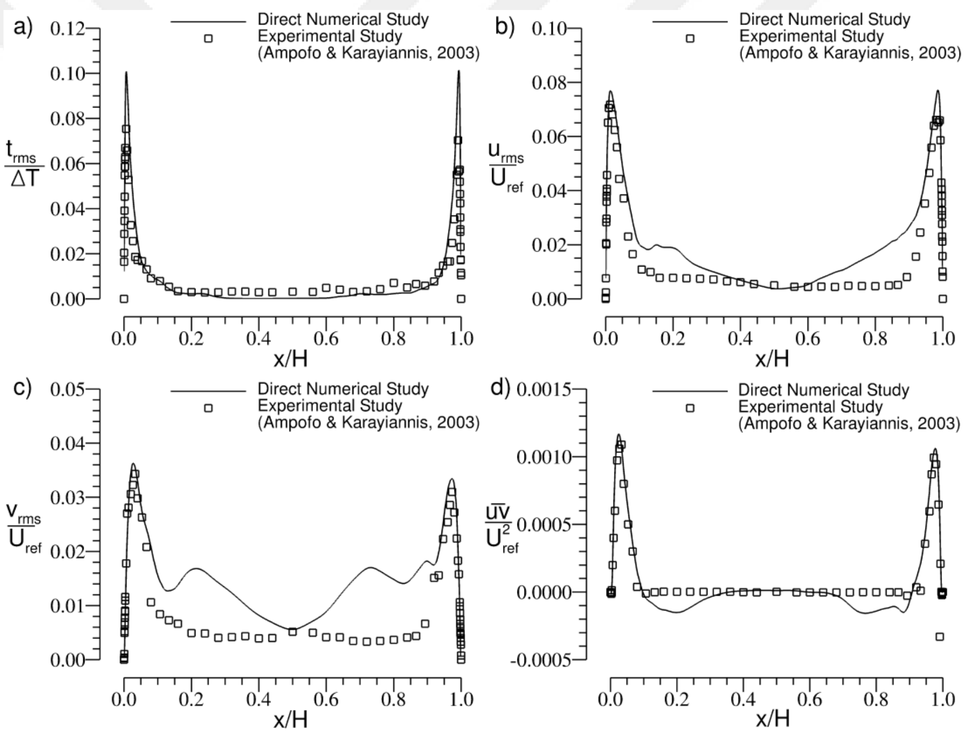

Figure 3.3 Second order statistics validation of the numerical study

3.6 Independence of the Vortex Eduction Method

Even though there is no universally accepted definition of vortex, one of the widely known definition is that circular or spiral instantaneous streamwise pattern can be observed onto the normal plane when the reference frame moving with the center of vortex core (Robinson, 1991; Zhou, Adrian, Balachandar & Kendall, 1999). Vortex is not a mathematical property such as vorticity but it is a topological structure that also highly related to flow properties. On the other hand, coherent vortical structure is a vortex that can be observed long enough. Another definition of the coherent vortical structure is that one or more properties (such as velocity component, pressure, temperature, etc) are correlated itself or another over a space or time (Robinson, 1991).

The challenge of identification vortex core has lead to the number of different techniques. The early strategy of identification vortex relied on the low- and high-pressure region where vortex core source a low-pressure whereas high-pressure regions induced by nearby vortex (Robinson, 1991; Singer & Joslin, 1994). However, the interaction of various vortex core distorted low-pressure criteria, and this opens the question to the reliability of this method (Villiers, 2006). The streamlines are another early criteria for the identification of vortices but it relies on the reference frame, not Galilean invariant. In other words, the vortex can be observed in one reference frame but it cannot be seen in another moving frame (Villiers, 2006). However, this technique has still be used with assisted another flow property. The particle image velocimeter (PIV) frame convected a certain speed that the vortex pattern makes circular on the region of local maximum vorticity (Adrian, Meinhart & Tomkins, 2000). However, the maximum vorticity is not only coincided with the vortex but also contains the shear flow. Another criterion is the vorticity line, defined parallel to the vorticity vector, may address the identification but it is susceptible to misleading traces of vortex core (Robinson, 1991). Some modern techniques are successfully identified of the vortex core, and also these are Galilean invariant. However, they have also their limitations (Zhou et al., 1999).

The velocity gradient tensor defined as,

$$\nabla\boldsymbol{u} = \begin{bmatrix} \frac{\partial u}{\partial x} & \frac{\partial u}{\partial y} & \frac{\partial u}{\partial z} \\ \frac{\partial v}{\partial x} & \frac{\partial v}{\partial y} & \frac{\partial v}{\partial z} \\ \frac{\partial w}{\partial x} & \frac{\partial w}{\partial y} & \frac{\partial w}{\partial z} \end{bmatrix} \tag{3.9}$$

The characteristic equation of the velocity gradient tensor, $\nabla\boldsymbol{u}$, reads (Chong, Perry, & Cantwell, 1990),

$$\lambda^3 + P\lambda^2 + Q\lambda + R = 0 \tag{3.10}$$

where P is the first invariant, P = $-\nabla.\boldsymbol{u}$, R is the third invariant, R = -determinant($\nabla\boldsymbol{u}$), and Q is the second invariant as shown (Hunt, Wray & Moin, 1988) ,

$$Q = \frac{1}{2}(\boldsymbol{\Omega}^2 - \boldsymbol{S}^2) \tag{3.11}$$

where anti-symmetric component of $\nabla\boldsymbol{u}$ which is represents the rotational rates,

$$\boldsymbol{\Omega}^2 = \Omega_{ij}\Omega_{ij} \tag{3.12}$$

and symmetric component of $\nabla\boldsymbol{u}$ which is represents the strain rates,

$$\boldsymbol{S}^2 = S_{ij}S_{ij} \tag{3.13}$$

The positive Q-criteria indicates the rotational rates overcomes to the rates of strain (Villiers, 2006; Dubief & Delcayre, 2000). In other words, the anti-symmetric tensor proportional to the enstrophy density while the symmetric tensor proportional to the dissipation of kinetic energy (Alfonsi, 2006). The positive Q-criteria can identify the vortex core with an additional condition that is the minimum local pressure (Alfonsi, 2006).

Other criteria was proposed based on the second largest eigenvalue of $\boldsymbol{\Omega}^2 + \boldsymbol{S}^2$ (Jeong & Hussain, 1995). This method identifies vortex core without explicitly restrict the local pressure. A local minimum pressure exists if $\boldsymbol{\Omega}^2 + \boldsymbol{S}^2$ has two negative eigenvalues (Dubief & Delcayre, 2000). The eigenvalues of the symmetric tensor, $\boldsymbol{\Omega}^2 + \boldsymbol{S}^2$, is a real only if $\lambda_1 \leq \lambda_2 \leq \lambda_3$, and a vortex core can be identified if the second eigenvalues of the $\boldsymbol{\Omega}^2 + \boldsymbol{S}^2$ is negative, $\lambda_2 < 0$ (Villiers, 2006).

Q is the second invariant where difference to the rotational rates and the strain rates. The positive Q-criteria indicates the rotational rates (Ω) overcomes to the rates of strain(S) (Villiers, 2006; Dubief & Delcayre; 2000). In other words, the anti-symmetric tensor proportional to the enstrophy density while the symmetric tensor proportional to the dissipation of kinetic energy (Alfonsi, 2006). The positive Q-criteria can identify the vortex core with an additional condition that is the minimum local pressure (Alfonsi, 2006). Other criteria was proposed based on the second largest eigenvalue of $\boldsymbol{\Omega}^2 + S^2$ (Jeong & Hussain, 1995). This method identifies vortex core without explicitly restrict the local pressure. A local minimum pressure exists if $\boldsymbol{\Omega}^2 + S^2$ has two negative eigenvalues19. The eigenvalues of the symmetric tensor, $\boldsymbol{\Omega}^2 + S^2$, is a real only if $\lambda_1 \geq \lambda_2 \geq \lambda_3$, and a vortex core can be identified if the second eigenvalues of the $\boldsymbol{\Omega}^2 + S^2$ is negative, $\lambda_2 < 0$ (Villiers, 2006).

Another frame independence criterion is a local *swirling strength* to identified vortical structures. The imaginary part of the complex eigenvalue of the velocity gradient tensor, λ_{ci}, represents circular motion vicinity of the vortex core (O'Farrell, & Martín, 2009). The discriminant of $\nabla\boldsymbol{u}$ shown,

$$\Delta = \left(\frac{1}{3}\tilde{Q}\right)^3 + \left(\frac{1}{3}\tilde{R}\right)^2 \tag{3.14}$$

where $\tilde{R} = R + \frac{2}{27}P^3 - \frac{1}{3}P$, and $\tilde{Q} = Q - \frac{1}{3}P^2$ (Zhou et al., 1999; O'Farrell, & Martín, 2009). When $\Delta \leq 0$, three eigenvalues of $\nabla \boldsymbol{u}$ are real (Zhou et al., 1999; Alfonsi, 2006; O'Farrell, & Martín, 2009). When $\Delta > 0$, $\nabla \boldsymbol{u}$ has one real eigenvalue and two pairs of complex conjugated eigenvalues (Zhou et al., 1999; Alfonsi, 2006; O'Farrell, & Martín, 2009). The region where has two complex eigenvalues is represents sufficient conditions for vortex (Chong, Perry, & Cantwell, 1990). It is also suggested that this criterion should be supported intense vorticity magnitude region (Zhou et al., 1999).

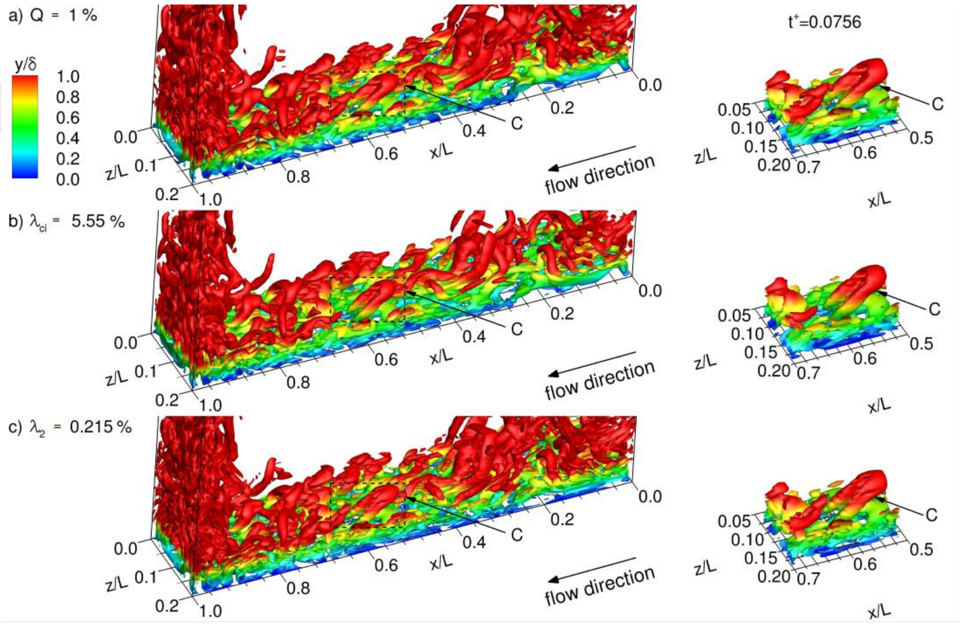

Figure 3.4 Independence of vortex eduction method

The independence of the vortex identification method has shown in Figure 3.4. The second invariant of velocity gradient (Q-criteria), swirling strength (λ_{ci}) and the second largest eigenvalue (λ_2-criteria) with negative value are presented in Figure 3.4a, 3.4b and 3.4c, respectively. The focused region, labeled C vortex, showed that even though some background noise or small vortical structures present small differences, each method with a certain threshold value can identify the C vortex. Overall, many coherent structures successfully captured each method and the difference is small. Therefore, these coherent structures are independence of the vortex eduction method, and they are intrinsic structures of this type of turbulent boundary layer.

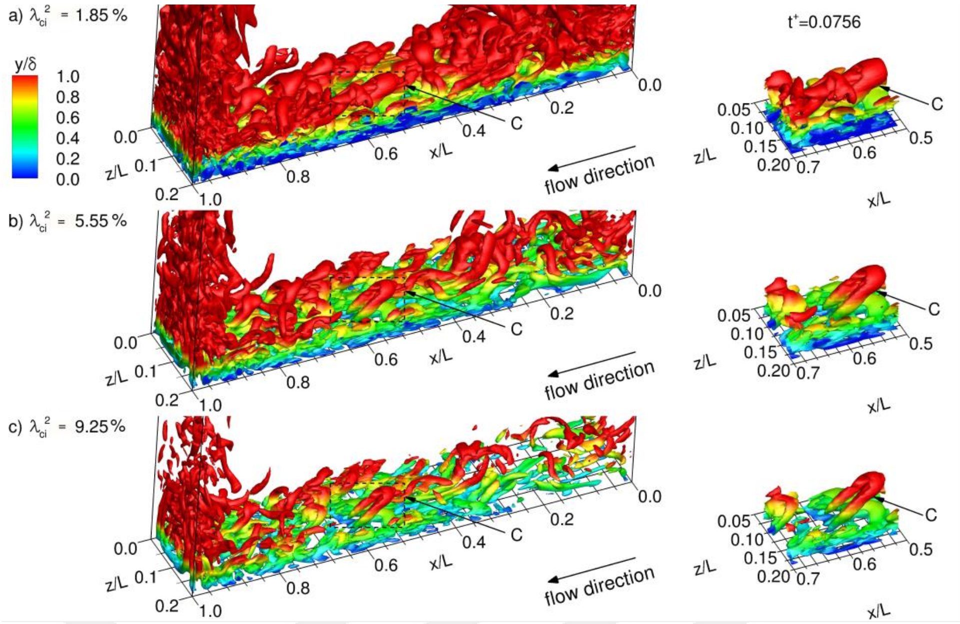

Figure 3.5 Independence of swirling strentgh (λ_{ci})

In this study, we have used the swirling strength to identify the vortical structures. Independence of swirling strength is presented extracted different threshold values on iso-surfaces (Figure 3.5). Figure 3.5a, 3.5b, and 3.5c represent an overall view of instantaneous vortical structures and close view of the labeled C vortex with three different threshold values %1.85, %5.55 and %9.25 of maximum swirling strength. Overall, it can be seen that the general topology of coherent vortical structures is the same with different threshold values, and the visualization of the vortical structures is independent of the threshold value. However, some topological different can be on threshold values. The smaller threshold value tends to the large size of vortex cores that also visualize smaller strength of vortices with background noise (non-coherent structures) whereas the larger threshold value leads to diminished or weakened of the vortex cores. Thus, the threshold value of the maximum swirling strength is chosen %5.55 to better visualize the vortices in this study.

3.6 Validation of the Turbulent Kinetic Energy Budgets Calculation

The relationship between the coherent vortical structures and the transport of the turbulent kinetic energy budget was investigated in this study. The turbulent budget equation reads (Komen et al., 2017),

$$\frac{\partial \overline{u_i u_j}}{\partial t} + u_k \frac{\partial \overline{u_i u_j}}{\partial x_k} = \overline{P_{ij}} + \overline{\epsilon_{ij}} + \overline{T_{ij}} + \overline{\pi_{ij}}^{s} + \overline{\pi_{ij}}^{d} + \overline{D_{ij}} \tag{3.15}$$

where turbulent kinetic energy shear production,

$$\overline{P_{ij}} = -\overline{u_j u_k}\frac{\partial \overline{u_i}}{\partial x_k} - \overline{u_i u_k}\frac{\partial \overline{u_j}}{\partial x_k} \tag{3.16}$$

the dissipation rate,

$$\overline{\epsilon_{ij}} = -2\nu \frac{\partial \overline{u_i}}{\partial x_k}\frac{\partial \overline{u_j}}{\partial x_k} \tag{3.17}$$

the turbulent transport rate,

$$\overline{T_{ij}} = -\frac{\partial \overline{u_k u_i u_j}}{\partial x_k} \tag{3.18}$$

the pressure strain rate,

$$\overline{\pi_{ij}}^{s} = -\frac{\overline{p}}{\rho}\left(\frac{\partial \overline{u_i}}{\partial x_j} - \frac{\partial \overline{u_j}}{\partial x_i}\right) \tag{3.19}$$

and molecular diffusion,

$$\overline{\pi_{ij}}^{d} = \frac{\partial}{\partial x_k}\left(\nu \frac{\partial \overline{u_i u_j}}{\partial x_k}\right) \tag{3.20}$$

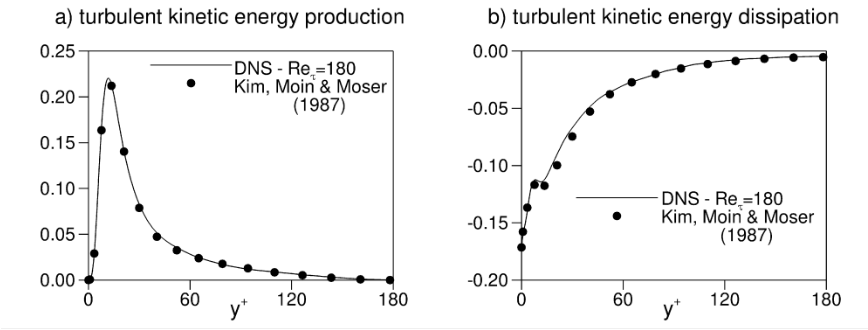

Figure 3.6 Validation of the turbulent kinetic energy budget calculation

Validation of the calculation of the turbulent kinetic energy budget is performed on turbulent channel flow at Reynolds number based on the friction velocity, Re_τ = 180 and statistical turbulent properties compared to Kim, Moin, and Moser (1978). The dimensions of the channel are 2π, π and 2 in streamwise, spanwise and wall-normal direction, respectively. The streamwise and spanwise direction of the channel assumed periodic boundary condition while wall-normal directions are imposed no-slip boundary conditions. The flow is driven by the pressure gradient in the channel flow and the Reynolds number based on the channel centerline velocity, Re_c = 3300. The structured finite volume grids are 256, 248 and 256 in the streamwise, spanwise and wall-normal direction. The distribution of grids is kept constant in the periodic streamwise and spanwise direction whereas the grid distribution is increased constantly from $y^+ < 1$ to $y^+ = 4.4$ until reached the center of channel height in the wall-normal direction. Initially, streaky flow is imposed the domain to accelerate the simulation based on the linear stability theory. The second ordered-central difference is used for convective and diffusion terms in the governing equation while the second-ordered backward difference is imposed for time-depending terms. Segregated Pressure Implicit with Splitting of Operator (PISO) algorithm is used to solve the pressure and velocity vectors with the open-source finite volume solver, OpenFOAM 5.x. As shown in Fig. 3.6, the turbulent kinetic energy production and dissipation term on the channel flow is excellent agreement with this computational method that applied to the turbulent cavity flow. Moreover, in this section, the calculation process of these budget terms also validated against the results of the turbulent channel flow at Re_τ = 180 by Kim, Moin, and Moser (1978), which used the spectral method.

CHAPTER FOUR
RESULTS AND DISCUSSION

4.1 Background: Theory of the Hairpin Vortex

Even though the turbulent flow is treated complex, chaotic, and randomness motion, some coherent structures can be observed long enough with various scale. These structures are not only basic building blocks of turbulent flow but also significantly contribute to shear force and heat transfer (Adrian 2007; Robinson, 1991). A coherent turbulent structure in the boundary layer is demonstrated by spanwise oriented vortex lines in a boundary layer (Figure 4.1a). This structure stretches and lifts away from the wall. The pattern of the vortex is identified as Λ or hairpin shaped. The hairpin vortex straddles the low-speed streak associated with quasi-streamwise vortices shown in Figure 4.1b (Adrian, 2007). The spanwise-oriented head of the hairpin-like vortex violently lifts away from the wall, encounter larger mean flow velocity and retards the background ($u < 0$ and $v > 0$, where u and v velocity are fluctuations in the streamwise and wall-normal direction, respectively) is also called ejection event (Adrian, 2007). Meanwhile, the ejection event feeds by legs and necks of the hairpin vortex from the high-speed streaky flow; fluid moves toward the wall referred to sweep event ($u > 0$ and $v < 0$) (Adrian, 2007). As basic building blocks of the turbulent boundary layer are hairpin vortices, the streamwise (u) and wall-normal (v) velocity fluctuation are correlated with each other, and more probability of u times v is negative (Figure 4.1c) (Adrian, 2007). Quadrant analysis is usually addressed to explain the role of the Reynolds stresses on the ejection and sweep events. The ejection events (the second quadrant of tangential Reynolds stresses) are generally observed stronger and higher speed than the sweep events (the fourth quadrant of tangential Reynolds stress) (Adrian, 2007) meanwhile high-speed streaks generally tend to be larger than the low-speed streaks (Jiménez, 2018).

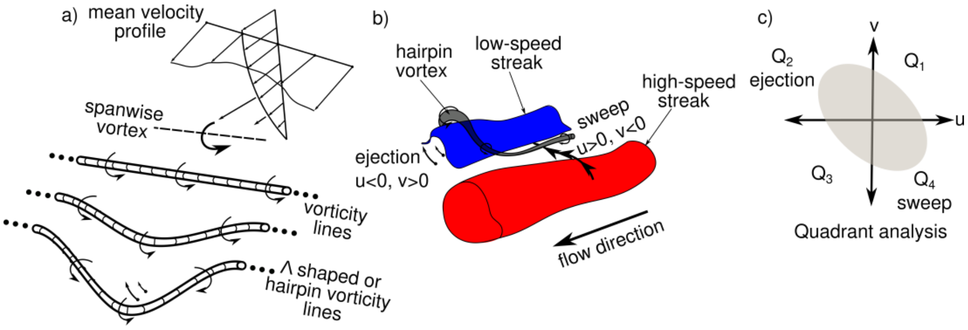

Figure 4.1 Schematic of a hairpin vortex theory

4.2 Theory of the Anti-Hairpin Vortex

The hairpin-like vortices are still dominant structures in the buoyancy-driven turbulent boundary layer and have similar features of the theory of hairpin vortex they nevertheless present distinguishable characters (Figure 4.2a). Merging mechanism of hairpin vortices could be many different configurations in the real turbulent boundary layer; however, three idealized possible merging mechanisms were presented by Tomkins & Adrian (2003). One of the proposed merging mechanism is the inner legs of the vortices join together in the spanwise direction, and the vortices growth with the annihilation of the inner legs and convect to one single larger vortex (Tomkins & Adrian 2003; Wark & Nagib, 1991). As shown those vortices labeled A in Figure 4.2b, two hairpin vortices interacted in the spanwise direction. While dimensionless time differences reached $t^+ = 0.061$ (Figure 4.2c), the inner legs cannot be identified, and the heads of the vortices came to the verge of the merge each other. At the final stage of the spanwise merging (Figure 4.2d), a larger hairpin vortex was formed with the annihilation of neighboring legs as proposed (Tomkins & Adrian, 2003). However, the process is not symmetric and identical. The selenoid effects, analogous magnetic flux induced by windings, can be observed in vortices labeled B (Figure 4.2a). In this model, the conceptual scenario of the nested packets of the hairpin vortices aligns in the streamwise direction and induced by combined vorticity core (Adrian, Meinhart & Tomkins, 2000). Another common feature is that the head of the quasi-streamwise vortex pair lifts away from the wall (Figure 4.2e); intermediate structures inclined about 45 degrees to the wall afterward (Figure 4.2f). The subsequent structure, is vortex labeled C, tends to curved vertical direction to the wall (Zhou, Adrian, Balachandar & Kendall, 1999) while moving downstream as well as becomes a mature hairpin vortex (Figure 4.2g). By t^+ = 0.160, the legs and necks of the hairpin vortex have a shallow angle to the wall while the head has a steeper inclination Zhou, Adrian, Balachandar & Kendall, 1999). The parent-offspring mechanism (or regeneration mechanism) of the hairpin vortex was also observed in Figure 4.2g. The process of replicate itself presented younger secondary hairpin vortex labeled c that straddled on the legs of the parent vortex labeled C at t^+ = 0.160 (Zhou, Adrian, Balachandar& Kendall, 1999; Panton, 2001).

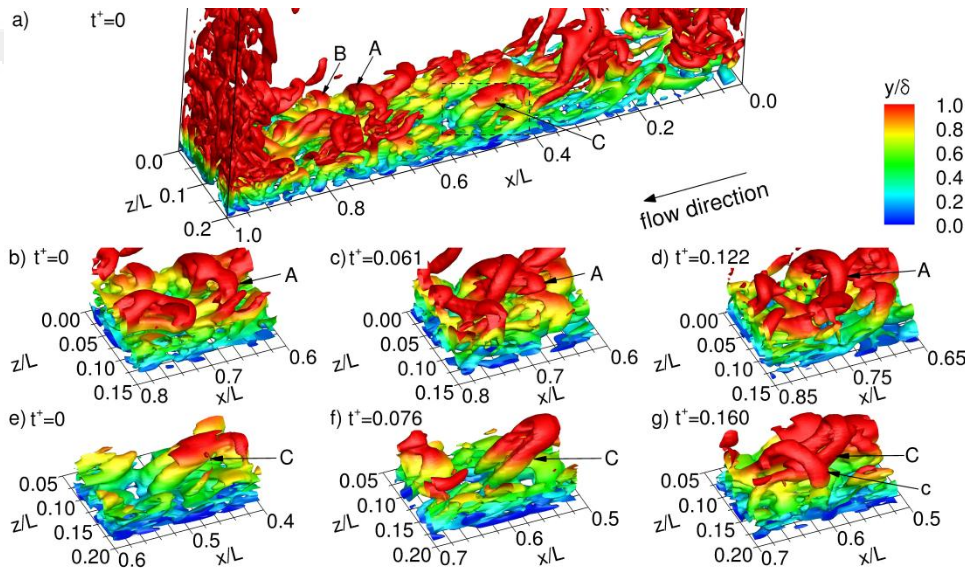

Figure 4.2 Vortex identification with isosurface of *swirling strength*

The hairpin vortices in the buoyancy-driven boundary layer have distinguishable features than the theory of hairpin vortex. The most striking feature of these hairpin vortices is point upstream direction instead of the downstream (Figure 4.2a). Because of this distinguishable character, the hairpin vortex in the buoyancy-driven turbulent boundary layer is named anti-hairpin vortex. Nevertheless, an upstream pointing of the hairpin vortex is observed in some previous studies, but this is not a common feature of them. One of the cases observed upstream pointed hairpin represented transitional flow induced by passing wakes (Wu, Jacobs, Hunt, & Durbin, 1999). A large-amplitude vertical velocity component in the free stream velocity triggered the transition flow that produced upstream pointed turbulent spots. The main motivation of this behavior was related to the source of the turbulence. It was suggested that the upstream pointed spot was triggered a turbulence source higher above the wall; otherwise, the spot was pointed downstream direction. In the case of the varicose-like breakdown (or symmetric breakdown), the hairpin vortex alternatively pointed upstream or downstream direction (Nishino, Hahn & Shariff, 2010). It was also observed hairpin vortices located above the legs of the upstream pointed hairpin vortex. It was suggested that interaction between high- and low-speed streaks play an important role in the formation of the hairpin vortex (Nishino, Hahn & Shariff, 2010). However, in both case could not explain anti-hairpin vortex, they had neither large-amplitude vertical velocity nor varicose-like breakdown triggered. Moreover, the upstream and downstream pointed vortex was not observed together in this study. Nonetheless, the case of the wall jet also produced an upstream pointed hairpin vortex, furthermore, most of the vortex pointed upstream in this case. The source of these vortices was related to coming from inside the turbulent jet region due to wall jet on the Coanda surface. Despite the other studies, there were striking similarities between the hairpin vortex from wall jet and buoyancy-driven boundary layer flows. The hairpin vortex straddled on the high momentum streaks and the most probability of velocity fluctuation in the quadrant analysis were first and third quadrant (Nishino, Hahn & Shariff, 2010). However, some unanswered questions have still existed about the source of these vortices, and it was also stated that the exact mechanism of the upstream pointed vortices was still unclear (Nishino, Hahn & Shariff, 2010). Moreover, we aim to explain which mechanism in the wall jet and buoyancy-driven boundary flow produce similar behaviour vortices.

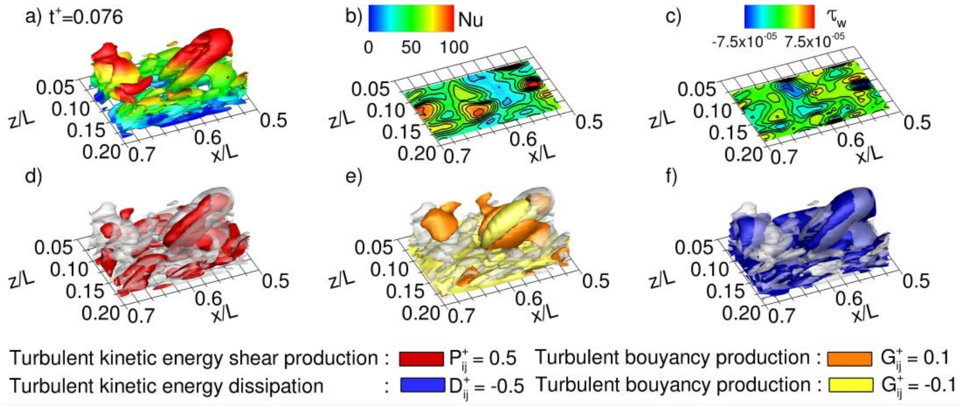

Figure 4.3 Isosurface of a) the *swirling strength*, b) Nusselt number at the hot wall, c) wall shear stress at the hot wall, d) turbulent kinetic energy shear production, e) turbulent kinetic energy buoyancy production, and f) turbulent kinetic energy dissipation

The anti-hairpin vortex in the buoyancy-driven turbulent boundary layer has a major responsibility of heat transfer, wall shear stress, and transport of the turbulent kinetic energy. For that reason, to identify and understand the dynamic of hairpin vortices are key to modeling and control of turbulent boundary flows (Schoppa & Hussain, 2002). As shown in Figure 4.3b, The heat transfer from the wall significantly increases the vicinity of the legs of the anti-hairpin vortex. The downwash flow near the exterior of the legs with sweep events brings the colder flow towards the wall (Sebilleau, Issa, Lardeau & Walker, 2018) while the upwash flow beneath the head of the vortex carries the hot plume away from the wall; therefore, the temperature gradient the vicinity of the anti-hairpin vortex remarkably increases. Similarly, downwash motion transport the high-speed fluid particle towards the wall as upwash motion transport low-speed fluids away from the wall; as a result, larger skin friction observed near the vortex (Figure 4.3c) (Kravchenko, Choi & Moin, 1993).

It is important to provide qualitative and high accuracy data of the transport equation for turbulent kinetic energy to better predict the turbulent(Sebilleau, Issa, Lardeau & Walker, 2018; Barhaghi& Davidson, 2007). In this study, instantaneous turbulent kinetic energy shear production, buoyancy production, and dissipation term investigated to understand the relationship between hairpin vortex and the budget terms of the turbulent kinetic energy. The turbulent kinetic energy dominated near the wall but the upwash flow of ejection events augmented the transport of turbulent kinetic energy production away from the wall where the $u \times u$ and velocity gradient is positive and negative, respectively, leads to positive hear production (Figure 4.3d). The buoyancy production term is important as shear production and the same order of magnitude to shea production (Barhaghi& Davidson, 2007) that leads to underpredict the turbulence kinetic energy and predict the erroneous location transition if omit the buoyancy term (Sebilleau, Issa, Lardeau & Walker, 2018; Barhaghi& Davidson, 2007). The maximum production of the buoyancy in the mean profile occurred very beginning of the velocity maximum (Barhaghi& Davidson, 2007). It is observed that positive buoyancy production is related to the downwash sweep events (Figure 4.3e). It can be related to colder air moves toward to wall. However, it is also observed the important magnitude of negative buoyancy production occurred in the ejection events that negative buoyancy could not be observed in the mean buoyancy production profile (Sebilleau, Issa, Lardeau & Walker, 2018; Barhaghi& Davidson, 2007). The negative magnitude of buoyancy production is the same magnitude of positive production, and it is important to take account in the turbulent model. The negative buoyancy production related to upwash motion of hotter air by ejection events. The dissipation term is a sink term in the turbulent kinetic energy budget and related to vorticity. The mean dissipation profile shows that dissipation is important near the wall (Sebilleau, Issa, Lardeau & Walker, 2018; Barhaghi& Davidson, 2007). However, the vortex core of the hairpin enlarged the dissipation also increase the influence away from the wall (Figure 4.3f).

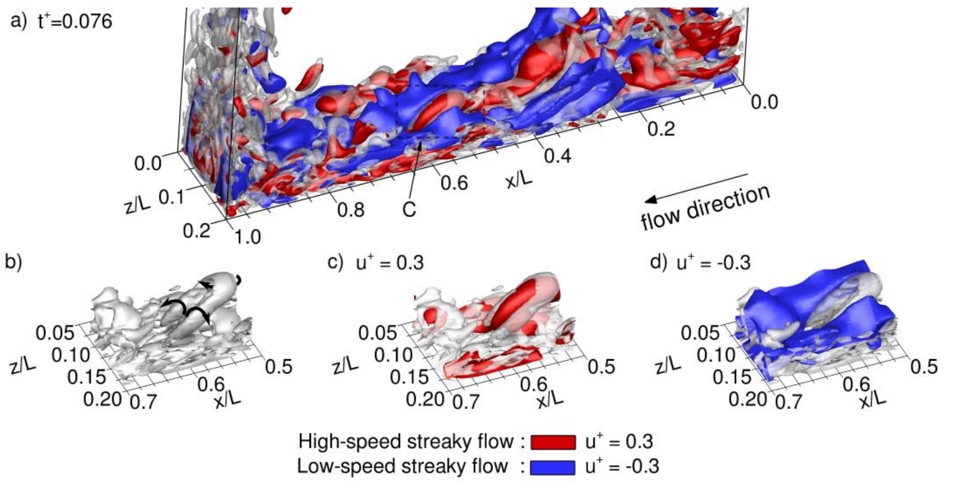

Figure 4.4 Identification of the high- and low-speed streaks with the anti-hairpin vortices

One of the well-known characteristics of the hairpin vortex is streaky flow. The long and narrow elongated region of streamwise velocity fluctuation (u) in the turbulent flow is defined streaks and observed all distance from the wall in the turbulent boundary layer (Jiménez, 2018). Low-speed streaks (u < 0) generally associate with streamwise oriented vortex pair, and the head of the vortex lifts away on the low-speed streak. Similarly, the buoyancy-driven turbulent flow contains the streaks and accommodates several vortices on them (Figure 4.4a). Low-speed streaks play an important role in the skin friction, transport of turbulent kinetic energy, and vortex generation for the canonical turbulent boundary layer flow (Adrian, 2007). In the case of the anti-hairpin vortices, the high-speed streak is a source of heat transfer (Figure 4.3b), skin friction (Figure 4.3c), turbulent kinetic energy productions (Figure 4.3d and Figure 4.3e), dissipation (Figure 4.3f), and the high-speed streaks also accommodate the several vortices (Figure 4.4a). As shown in Figure 4.3b, labeled C vortex lifted away from the wall as proposed the hairpin theory; however, the vortex straddled on the high-speed streak instead of the low-speed streak (Figure 4.4c), and low-speed streak engulfed the high-speed streak and the anti-hairpin vortex (Figure 4.4d). The low-speed streaks generally explained that a hairpin vortex lifts from the wall as slower fluid particle upwash that retards the background flows (Adrian, 2007). Whereas, the anti-hairpin vortex lifts away from the wall on the high-speed streaks, as well as, the head of the anti-hairpin vortex pushes the fluid particles to the downstream direction and accelerates it because of the orientation of the vortex (Figure 4.4v). Lastly, the high-speed streak generally tends to be larger than the low-speed streak in the canonical turbulent boundary layer (Jiménez, 2018), yet low-speed streak is observed larger than the high-speed streak in the buoyancy-driven turbulent boundary layer (Figure 4.4a).

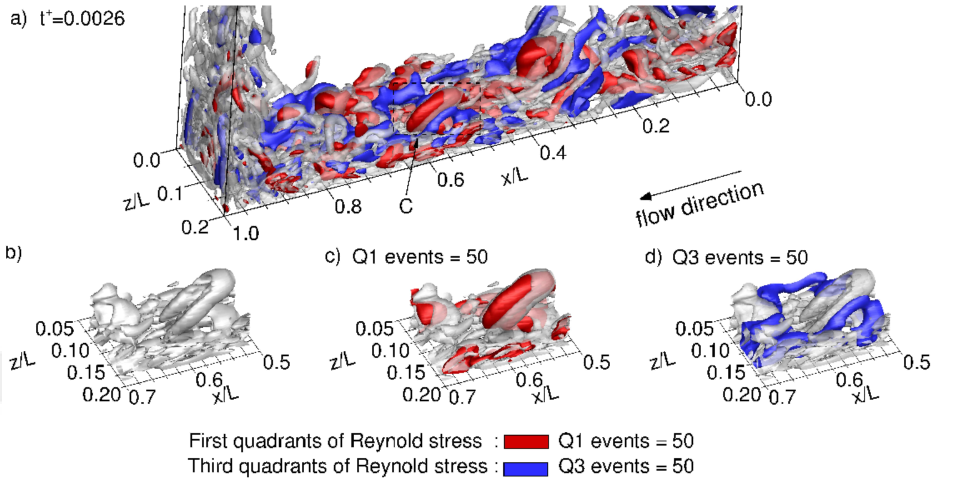

Figure 4.5 Tangential Reynolds stresses with anti-hairpin vortices

The early single-point experimental studies of hairpin vortices were inspected tangential Reynolds stresses in a wall-bounded turbulent boundary layer that was observed more probability of the second quadrant (related to the ejection event) and fourth quadrant (related to the sweep event) of the *u*-*v* plane, whereas these events are nowadays presenting three-dimensional structures in the modern computer era; these dominant events are the main source of the streamwise momentum exchange between the different layer of flow and turbulent drag (Jiménez, 2018). Unlike the behavior of tangential Reynolds stresses for the canonical turbulent boundary layer, the most dominant *u*-*v* correlation for the anti-hairpin vortices in the buoyancy-driven turbulent boundary layer are first and third quadrant of the *u*-*v* plane (Figure 4.5a) while the second and fourth quadrant of the tangential Reynolds stresses were found uncorrelated and unrelated to anti-hairpin vortices. In the theory of anti-hairpin vortex, the ejection event corresponds to the first quadrant of the Reynolds stresses instead of the second one, which carries fluid particles away from the wall (Figure 4.5c), whilst the sweep event corresponds to the third quadrant instead of the fourth one, that pushes the fluids toward to the wall (Figure 4.5d). Notwithstanding, the ejection and sweep events correspond to the different quadrants than the canonical turbulent boundary layer, the three-dimensional ejection event tends to more larger than the sweep event in both cases (Jiménez, 2018) that might be related to the ejection events supported by more extended duration sweep events, and the ejections tend to form in a (Adrian, 2007). Also, the ejection events focus in the concentrated region underneath of the head of the vortex as the sweep events prevail distributed region outboard of the vortex (Adrian, 2007). It is stated that the vortices take the energy from the shear with *u* times $v < 0$ and lose the energy with *u* times $v > 0$ in the canonical turbulent boundary layer (Jiménez, 2018). Because of the the most probability of correlated velocity component *u* times $v > 0$ (positive quadrants) instead of u times $v < 0$ (negative quadrant) in the anti-hairpin vortex theory, this behavior is expected to be opposite.

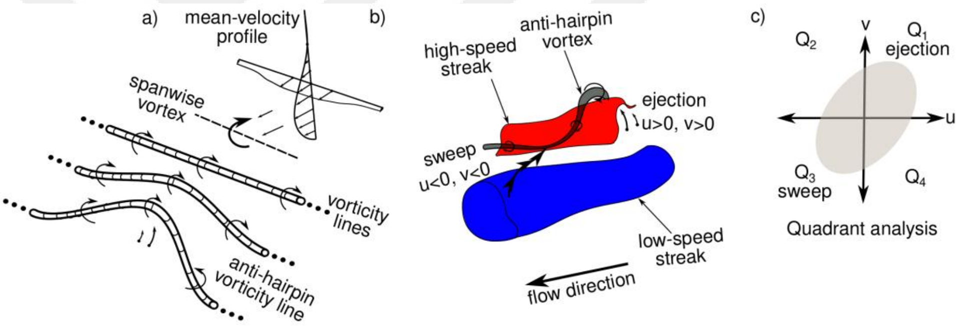

Figure 4.6 Schematic of anti-hairpin vortex theory

The typical coherent structures for buoyancy-driven turbulent boundary layer were observed anti-hairpin vortices which are pointed upstream direction that is intrinsic vortex behavior in this type of flows. The anti-hairpin vortex is originated dominant spanwise vortex located outer layer of the peak velocity in the mean velocity profile (Figure 4.6a). Subsequently, the spanwise vortex lifts away from the wall, pushes the fluid particle in the downstream direction ($u > 0$ and $v > 0$), is also related to the ejection events. Meanwhile, the ejections events feed by legs and necks of the anti-hairpin vortex from the low-speed streaks; fluid particle moves toward the wall referred to sweep events ($u < 0$ and $v < 0$). Not only the pattern of the vortex was V-shaped but also the characteristics were opposite to the hairpin vortex. The anti-hairpin vortex straddles on the high-speed streak and is opposite rotational direction than the hairpin vortex (Figure 4.6b). The most probability of *u*-*v* correlation is positive; the first quadrant related to the ejection whereas the third quadrant is related to the sweep event (Figure 4.6c). The ejection events are observed stronger and greater speed than the sweep events, meanwhile, low-speed streaks tend to be larger than the high-speed streaks.

Our observation also leads to two claims of the vortex dynamics in the turbulent flow. Firstly, the origin of the hairpin vortex or anti-hairpin vortex is related to the shear flow in the boundary layer. The profile of the shear influences on the features of the vortex. The statement that the shear flow is the source of turbulence is insufficient, the profile of the shear flow also significantly contribute to the shape and orientation of the vortex and alter the kinematics and energy carrying mechanism. Secondly, the transport phenomena and shear stress increase in the turbulent flow, which is explained turbulence mean profiles are more shallow than the laminar flows. In terms of the modeling of turbulence and interest in mean properties, this statement may be enough to explain the physics. But it hides the instantaneous mechanism of transport phenomena. In terms of the controlling turbulent and interest in the evolution of vortex, the instantaneous vortex dynamics may different than the mean one (i.e., the symmetric hairpin vortex is common in the mean calculations, but the anti-symmetric hairpin is more prevalent in real turbulent boundary layer). The coherent vortical structures significantly increase transport phenomena and shear stresses, whereas the absence of these coherent vortices, these phenomena remarkably reduced. This may be sign of the turbulent flow could have small shear stress and less transported strength as long as we achieve the control of these coherent vortical structures.

CHAPTER FIVE
CONCLUSION

Coherent vortical structures can be observed in the turbulent flow even though turbulent is considered the chaotic and random process. Theory of the hairpin vortex proposes generally downstream pointed vortex, which allows explaining kinematics, regeneration, energy-carrying mechanism, and dynamics of vortices. On the other hand, upstream pointed vortices are generally assumed exception of a certain situation and maybe observed together with downstream pointed vortices. Nevertheless, in the case of the wall jet, hairpin vortices consistency pointed the upstream direction, but the origin of these vortices remained unclear. Interestingly, we observed upstream pointed hairpin vortices, but not in the wall jet case, it is in the buoyancy-driven turbulent boundary layer. Moreover, the unified theory of upstream pointed vortices, the theory of the anti-hairpin vortex, has not established in the literature. Here we show the hairpin vortices consistency points the upstream direction, and this is an intrinsic behavior of the anti-hairpin vortices. The anti-hairpin vortex straddle on the high-speed streaks where surrounding low-speed streaks. The lift-up process of the anti-hairpin vortex head, ejection event, is found in the first quadrant of the tangential Reynolds stress while sweep event is related to the third quadrant of the tangential Reynolds stress. We anticipate our results improve the understanding of the vortex behavior in the turbulent flows. Furthermore, the name of the anti-hairpin vortex is not only given for opposite behavior of the vortices but also this finding may contribute to control of the turbulent flows.

REFERENCES

Adrian, R. J. (2007). Hairpin vortex organization in wall turbulence. *The Physics of Fluids*, *19*(4), 041301.

Adrian, R. J., Meinhart, C. D., & Tomkins, C. D. (2000). Vortex organization in the outer region of the turbulent boundary layer. *Journal of Fluid Mechanics*, *422*, 1-54.

Alfonsi, G. (2006). Coherent structures of turbulence: methods of eduction and results. *Applied Mechanics Reviews*, *59*(6), 307-323.

Ampofo, F., & Karayiannis, T. G. (2003). Experimental benchmark data for turbulent natural convection in an air filled square cavity. *International Journal of Heat and Mass Transfer*, *46*(19), 3551-3572.

Asai, M., & Nishioka, M. (1989). Origin of the peak-valley wave structure leading to wall turbulence. *Journal of Fluid Mechanics, 208*, 1-23.

Azih, C., Brinkerhoff, J. R., & Yaras, M. I. (2012). Direct numerical simulation of convective heat transfer in a zero-pressure-gradient boundary layer with supercritical water. *Journal of Thermal Science*, *21*(1), 49-59.

Barhaghi, D. G., & Davidson, L. (2007). Natural convection boundary layer in a 5: 1 cavity. *The Physics of Fluids*, *19*(12), 125106.

Braga, S. L., & Viskanta, R. (1992). Transient natural convection of water near its density extremum in a rectangular cavity. *International Journal of Heat and Mass Transfer*, 35(4), 861-875.

Brinkerhoff, J. R., & Yaras, M. I. (2014). Numerical investigation of the generation and growth of coherent flow structures in a triggered turbulent spot. *Journal of Fluid Mechanics*, *759*, 257-294.

Brinkerhoff, J. R., & Yaras, M. I. (2015). Numerical investigation of transition in a boundary layer subjected to favourable and adverse streamwise pressure gradients and elevated free stream turbulence. *Journal of Fluid Mechanics*, *781*, 52-86.

Corino, E. R., & Brodkey, R. S. (1969). A visual investigation of the wall region in turbulent flow. *Journal of Fluid Mechanics*, *37*(01), 1-30.

Chenoweth, D. R., & Paolucci, S. (1986). Natural convection in an enclosed vertical air layer with large horizontal temperature differences. *Journal of Fluid Mechanics*, *169*, 173-210.

Choi, H., & Moin, P. (1994). Effects of the computational time step on numerical solutions of turbulent flow. *Journal of Computational Physics*, *113*(1), 1-4.

Chong, M. S., Perry, A. E., & Cantwell, B. J. (1990). A general classification of three-dimensional flow fields. *Physics of Fluids A: Fluid Dynamics*, *2*(5), 765-777.

Chung, Y. J., Yang, S. H., Kim, H. C., & Zee, S. Q. (2004). Thermal hydraulic calculation in a passive residual heat removal system of the SMART-P plant for forced and natural convection conditions. *Nuclear Engineering and Design*, *232*(3), 277-288.

Gad-El-Hak, M., Blackwelderf, R. F., & Riley, J. J. (1981). On the growth of turbulent regions in laminar boundary layers. *Journal of Fluid Mechanics*, *110*, 73-95.

de Vahl Davis, G. (1983). Natural convection of air in a square cavity: a bench mark numerical solution. *International Journal for Numerical Methods in Fluids*, 3(3), 249-264.

Dubief, Y., & Delcayre, F. (2000). On coherent-vortex identification in turbulence. *Journal of turbulence*, *1*(1), 011-011.

Fedorovich, E., & Shapiro, A. (2009). Turbulent natural convection along a vertical plate immersed in a stably stratified fluid. *Journal of Fluid Mechanics*, 636, 41-57.

Ganapathisubramani, B., Longmire, E. K., & Marusic, I. (2003). Characteristics of vortex packets in turbulent boundary layers. *Journal of Fluid Mechanics*, 478, 35-46.

Georgiadis, N. J., Rizzetta, D. P., & Fureby, C. (2010). Large-eddy simulation: current capabilities, recommended practices, and future research. *AIAA Journal*, 48(8), 1772-1784.

Goldstein, M. E., & Hultgren, L. S. (1989). Boundary-layer receptivity to long-wave free- stream disturbances. *Annual Review of Fluid Mechanics*, 21(1), 137-166.

Hack, M. P., & Moin, P. (2018). Coherent instability in wall-bounded shear. *Journal of Fluid Mechanics*, 844, 917-955.

Henningson, D., Spalart, P., & Kim, J. (1987). Numerical simulations of turbulent spots in plane Poiseuille and boundary-layer flow. *ThePhysics of Fluids*, 30(10), 2914-2917.

Herbert, T. (1983). Secondary instability of plane channel flow to subharmonic three-dimensional disturbances. *The Physics of Fluids*, 26(4), 871-874.

Hunt, J. C., Wray, A. A., & Moin, P. (1988). Eddies, streams, and convergence zones in turbulent flows. *Center of Turbulence Research Proceedings of the Summer Program*, *N89*, 24555

Inaba, H., & Fukuda, T. (1984). Natural convection in an inclined square cavity in regions of density inversion of water. *Journal of Fluid Mechanics*, *142*, 363-381.

Incropera, F. P. (1988). Convection heat transfer in electronic equipment cooling. *Journal of Heat Transfer*, *110(4b)*, 1097-1111.

Ivey, G. N. (1984). Experiments on transient natural convection in a cavity. *Journal of Fluid Mechanics*, *144*, 389-401.

Jasak, H., Jemcov, A., & Tukovic, Z. (2007a, September). OpenFOAM: A C++ library for complex physics simulations. *In International Workshop on Coupled Methods in Numerical Dynamics*. IUC Dubrovnik Croatia, pp. 1–20.

Jasak, H., Jemcov, A., & Maruszewski, J. P. (2007b, May). Preconditioned linear solvers for large eddy simulation. *In CFD 2007 Conference, CFD Society of Canada*. (https://www.bib.irb.hr/713776)

Jeong, J., & Hussain, F. (1995). On the identification of a vortex. *Journal of fluid mechanics*, *285*, 69-94.

Jemcov, A., Maruszewski, J. P., & Jasak, H. (2007, January). Performance improvement of algebraic multigrid solver by vector sequence extrapolation. *In CFD 2007 Conference, CFD Society of Canada*.

Jiménez, J. (2018). Coherent structures in wall-bounded turbulence. *Journal of Fluid Mechanics*, *842*.

Kachanov, Y. S. (1994). Physical mechanisms of laminar-boundary-layer transition.

Annual Review of Fluid Mechanics, *26*(1), 411-482.

Kim, J., Moin, P., & Moser, R. (1987). Turbulence statistics in fully developed channel flow at low Reynolds number. *Journal of fluid mechanics*, *177*, 133-166.

Kizildag, D., Trias, F. X., Rodríguez, I., & Oliva, A. (2014). Large eddy and direct numerical simulations of a turbulent water-filled differentially heated cavity of aspect ratio 5. *International Journal of Heat and Mass Transfer*, *77*, 1084-1094.

Kogawa, T., Okajima, J., Komiya, A., Armfield, S., & Maruyama, S. (2016). Large eddy simulation of turbulent natural convection between symmetrically heated vertical parallel plates for water. *International Journal of Heat and Mass Transfer*, *101*, 870-877.

Komen, E. M. J., Camilo, L. H., Shams, A., Geurts, B. J., & Koren, B. (2017). A quantification method for numerical dissipation in quasi-DNS and under-resolved DNS, and effects of numerical dissipation in quasi-DNS and under-resolved DNS of turbulent channel flows. *Journal of Computational Physics*, *345*, 565-595.

Klebanoff, P. S., Tidstrom, K. D., & Sargent, L. M. (1962). The three-dimensional nature of boundary-layer instability.*Journal of Fluid Mechanics*, *12*(1), 1-34.

Kravchenko, A. G., Choi, H., & Moin, P. (1993). On the relation of near-wall streamwise vortices to wall skin friction in turbulent boundary layers. *Physics of Fluids A: Fluid Dynamics*, *5*(12), 3307-3309.

Lankford, K. E., & Bejan, A. (1986). Natural convection in a vertical enclosure filled with water near 4 C. *Journal of Heat Transfer*, *108*(4), 755-763.

Lau, G. E., Yeoh, G. H., Timchenko, V., & Reizes, J. A. (2013). Large-eddy simulation of turbulent buoyancy-driven flow in a rectangular cavity. *International Journal of Heat and Fluid Flow*, *39*, 28-41.

Lee, S. D., Lee, J. K., & Suh, K. Y. (2007). Natural convection thermo fluid dynamics in a volumetrically heated rectangular pool. *Nuclear Engineering and Design*, *237*(5), 473-483.

Lozano-Durán, A., Flores, O., & Jiménez, J. (2012). The three-dimensional structure of momentum transfer in turbulent channels. *Journal of Fluid Mechanics*, *694*, 100-130.

Lozano-Durán, A., & Jiménez, J. (2014). Time-resolved evolution of coherent structures in turbulent channels: characterization of eddies and cascades. *Journal of Fluid Mechanics*, *759*, 432-471.

Markatos, N. C., & Pericleous, K. A. (1984). Laminar and turbulent natural convection in an enclosed cavity. *International Journal of Heat and Mass Transfer*, *27*(5), 755-772.

Miroshnichenko, I. V., & Sheremet, M. A. (2018). Turbulent natural convection heat transfer in rectangular enclosures using experimental and numerical approaches: A review. *Renewable and Sustainable Energy Reviews*, *82*, 40-59.

Morkovin, M. V. (1969). On the many faces of transition. *In Viscous Drag Reduction1*-31. US, Springer.

Ng, C. S., Ooi, A., Lohse, D., & Chung, D. (2017). Changes in the boundary-layer structure at the edge of the ultimate regime in vertical natural convection. *Journal of Fluid Mechanics*, *825*, 550-572.

Nishino, T., Hahn, S., & Shariff, K. (2010). Large-eddy simulations of a turbulent Coanda jet on a circulation control airfoil. *The Physics of Fluids*, *22*(12), 125105.

Elder, J. W. (1965). Turbulent free convection in a vertical slot. *Journal of Fluid Mechanics*, *23*(1), 99-111.

Emmons, HW. (1951). The laminar-turbulent transition in a boundary layer-Part I. *Journal of the Aeronautical Sciences*, *18*(7), 490-498.

O'Farrell, C., & Martín, M. P. (2009). Chasing eddies and their wall signature in DNS data of turbulent boundary layers. *Journal of Turbulence*, (10), N15.

Pallares, J., Vernet, A., Ferre, J. A., & Grau, F. X. (2010). Turbulent large-scale structures in natural convection vertical channel flow. *International Journal of Heat and Mass Transfer*, *53*(19-20), 4168-4175.

Panton, R. L. (2001). Overview of the self-sustaining mechanisms of wall turbulence. *Progress in Aerospace Sciences*, *37*(4), 341-383.

Patankar, S. V., Transfer, N. H., & Flow, F. (1980). *Hemisphere*. New York.

Perry, A. E., & Chong, M. S. (1982). On the mechanism of wall turbulence. *Journal of Fluid Mechanics*, *119*, 173-217.

Perry, A. E., Lim, T. T., & Teh, E. W. (1981). A visual study of turbulent spots. *Journal of Fluid Mechanics*, *104*, 387-405.

Pope, S. B. (2000). *Turbulent flows*. Cambridge, UK: Cambridge Univ. Press.

Reed, H. L., & Saric, W. S. (1989). Stability of three-dimensional boundary layers. *Annual Review of Fluid Mechanics*, *21*(1), 235-284.

Reinink, S. K., & Yaras, M. I. (2015). Study of coherent structures of turbulence with large wall-normal gradients in thermophysical properties using direct numerical simulation. *The Physics of Fluids*, *27*(6), 065113.

Reynolds, O. (1883). An experimental investigation of the circumstances which determine whether the motion of water shall be direct or sinuous, and of the law of resistance in parallel channels. *Proceedings of The Royal Society of London*, *35*(224-226), 84-99.

Robinson, S. K. (1991). Coherent motions in the turbulent boundary layer. *Annual Review of Fluid Mechanics*, *23*(1), 601-639.

Saric, W. S., Reed, H. L., & Kerschen, E. J. (2002). Boundary-layer receptivity to freestream disturbances. *Annual Review of Fluid Mechanics*, *34*(1), 291-319.

Sebilleau, F., Issa, R., Lardeau, S., & Walker, S. P. (2018). Direct Numerical Simulation of an air-filled differentially heated square cavity with Rayleigh numbers up to 10^{11}. *International Journal of Heat and Mass Transfer*, *123*, 297-319.

Shepard, E. L., Ross, A. N., & Portugal, S. J. (2016). Moving in a moving medium: new perspectives on flight, *Philosophical Transactions of the Royal Society B: Biological Sciences*, *371*, 201503.

Schoppa, W., & Hussain, F. (2002). Coherent structure generation in near-wall turbulence. *Journal of Fluid Mechanics*, *453*, 57-108.

Schöpf, W., & Patterson, J. C. (1995). Natural convection in a side-heated cavity: visualization of the initial flow features. *Journal of Fluid Mechanics*, *295*, 357-379.

Schubauer, G. B., & Harold, K. S. (1948) Laminar-boundary-layer oscillations and transition on a flat plate. No. NACA-909. *National Aeronautics and Space Administration (NASA)*, Washington DC.

Schubauer, G. B., & Klebanoff, P. S. (1955). Contributions on the mechanics of boundary-layer transition. *National Aeronautics and Space Administration (NASA)*, Washington DC, Technical Note, 3989.

Singer, B. A., & Joslin, R. D. (1994). Metamorphosis of a hairpin vortex into a young turbulent spot. *The Physics of Fluids*, *6*(11), 3724-3736.

Singer, B. A. (1996). Characteristics of a young turbulent spot. *The Physics of Fluids*, *8*(2), 509-521.

Smith, C. R., & Metzler, S. P. (1983). The characteristics of low-speed streaks in the near-wall region of a turbulent boundary layer. *Journal of Fluid Mechanics*, *129*, 27-54.

Tian, Y. S., & Karayiannis, T. G. (2000a). Low turbulence natural convection in an air filled square cavity: part I: the thermal and fluid flow fields. *International Journal of Heat and Mass Transfer*, *43*(6), 849-866.

Tian, Y. S., & Karayiannis, T. G. (2000b). Low turbulence natural convection in an air filled square cavity: Part II: the turbulence quantities. *International Journal of Heat and Mass Transfer*, *43*(6), 867-884.

Tomkins, C. D., & Adrian, R. J. (2003). Spanwise structure and scale growth in turbulent boundary layers. *Journal of Fluid Mechanics*, *490*, 37-74.

Trias, F. X., Soria, M., Oliva, A., & Pérez-Segarra, C. D. (2007). Direct numerical simulations of two-and three-dimensional turbulent natural convection flows in a differentially heated cavity of aspect ratio 4. *Journal of Fluid Mechanics*, *586*, 259-293.

Trias, F. X., Gorobets, A., Soria, M., & Oliva, A. (2010a). Direct numerical simulation of a differentially heated cavity of aspect ratio 4 with Rayleigh numbers up to 1011–Part I: Numerical methods and time-averaged flow. *International Journal of Heat and Mass Transfer*, *53*(4), 665-673.

Trias, F. X., Gorobets, A., Soria, M., & Oliva, A. (2010b). Direct numerical simulation of a differentially heated cavity of aspect ratio 4 with Rayleigh numbers up to 1011–Part II: Heat transfer and flow dynamics. *International Journal of Heat and Mass Transfer*, *53*(4), 674-683.

Xin, S., & Le Quéré, P. (1995). Direct numerical simulations of two-dimensional chaotic natural convection in a differentially heated cavity of aspect ratio 4. *Journal of Fluid Mechanics*, *304*, 87-118.

Wark, C. E., & Nagib, H. M. (1991). Experimental investigation of coherent structures in turbulent boundary layers. Journal of Fluid Mechanics, *230*, 183-208.

Wu, X., Jacobs, R. G., Hunt, J. C., & Durbin, P. A. (1999). Simulation of boundary layer transition induced by periodically passing wakes. *Journal of Fluid Mechanics*, *398*, 109- 153.

Wu, X., Moin, P., Adrian, R. J., & Baltzer, J. R. (2015). Osborne Reynolds pipe flow: Direct simulation from laminar through gradual transition to fully developed turbulence. *Proceedings of the National Academy of Sciences*, *112*(26), 7920-7924.

Wark, C. E., & Nagib, H. M. (1991). Experimental investigation of coherent structures in turbulent boundary layers. *Journal of Fluid Mechanics*, *230*, 183-208.

Wu, X., Jacobs, R. G., Hunt, J. C., & Durbin, P. A. (1999). Simulation of boundary layer transition induced by periodically passing wakes. *Journal of Fluid Mechanics*, *398*, 109- 153.

Wu, X., Moin, P., Adrian, R. J., & Baltzer, J. R. (2015). Osborne Reynolds pipe flow: Direct simulation from laminar through gradual transition to fully developed turbulence. *Proceedings of the National Academy of Sciences*, *112*(26), 7920-7924.

Versteegh, T. A. M., & Nieuwstadt, F. T. M. (1998). Turbulent budgets of natural convection in an infinite, differentially heated, vertical channel. *International Journal of Heat and Fluid Flow*, *19*(2), 135-149.

Villiers, E. (2006). The potential of large eddy simulation for the modeling of wall bounded flows. *Imperial College of Science, Technology and Medicine, London (UK).*

Yaras, M. I. (2007). An experimental study of artificially-generated turbulent spots under strong favorable pressure gradients and freestream turbulence. *Journal of Fluids Engineering*, *129*(5), 563-572.

Zhang, Z., Chen, W., Zhu, Z., & Li, Y. (2014). Numerical exploration of turbulent air natural-convection in a differentially heated square cavity at Ra= 5.33× 10 9. Heat and Mass Transfer, *50*(12), 1737-1749.

Zhou, J., Adrian, R. J., Balachandar, S., & Kendall, T. M. (1999). Mechanisms for generating coherent packets of hairpin vortices in channel flow. *Journal of Fluid Mechanics*, *387*, 353-396.